UNIVERSITY OF NAPLES "FEDERICO II"

Department of Chemical, Materials and Production Engineering

in partnership with

Procter & Gamble

DISSOLUTION OF CONCENTRATED SURFACTANT PASTE FROM MICRO TO PILOT PLANT SCALE

Ph.D. Student

Rosa Ilaria Castaldo

Academic Tutor:

Stefano Guido

Sergio Caserta

P&G Sponsors:

Chong Gu

Vincenzo Guida

Ph.D. in Industrial Product and Process Engineering

XXXI cycle

Table of Contents

Abstract 6

Introduction 8

I Surfactants 8

Characteristic of surfactants 11

Surfactants phase behavior characterization 16

Dissolution 20

Kinetic of surfactants dissolution 21

II Sodium Lauryl Ether 3 Sulfate 26

LAS/AES/H_2O phase diagram 28

III Aim of this work 29

CHAPTER 1 32

Dissolution of concentrated surfactant solutions: from microscopy imaging to rheological measurements through numerical simulations. 32

1.1 Abstract 33

1.2 Introduction 33

1.3 Materials and methods 36

Rheological setup 36

Optical setup 37

Numerical model 38

1.4 Results 41

Sample characterization 41

Optical experiments 44

Experimental data fit 46

Dynamic rheological experiments 47

1.5 Conclusions 50

1.6 Supplementary 51

CHAPTER 2 53

Experimental investigation of Surfactant Dissolution by direct visualization time-lapse microscopy. Anomalous diffusion mechanisms during surfactant dissolution. 53

2.1 Introduction 54

2.2 Materials and methods 55
Materials 55
Experimental setup 56
Time lapse microscopy 56
Sample description 57
2.3 Results 59
2.4 Conclusions 73
CHAPTER 3 74
Dissolution of complex surfactant paste under controlled microfluidic flow 74
3.1 Introduction 75
3.2 Materials and methods 76
Materials 76
Experimental setup 77
Time lapse microscopy 80
Rheology 81
Data analysis 87
3.3 Results 88
Flow test results 88
3.4 Conclusions 94
3.5 Supplementary 95
CHAPTER 4 98
Scale up of dissolution processes from microfluidics to pilot plant. 98
4.1 Introduction 99
4.2 Materials and methods 99
Materials 99
Experimental setup 99
4.3 Results 103
Conductibility measure results 103
Lab test results 105
Raman results 107
Pilot plant tests 108

Scale up results....109
4.4 Conclusions.... 111
Conclusions.... 113
Future work....116
Appendix.... 118
Conductivity and spectrophotometry measurements....118
Conductivity measurement....118
Spectrophotometry measurements....119
Analysis of dissolution experiments....121
Conductivity results....122
Spectrophotometry results....123
PCA analysis results....124
Conductivity vs Spectrophotometry....125
Dissolution test results....126
List of figures.... 128
References.... 131

Abstract

Complex fluids, widely used in many industrial applications, typically include amphiphilic molecules such as surfactants. Most of the surfactants used in products for fabric care, home care, and beauty care, such as detergents, or cosmetics have a complex microstructure and rheological behavior. At high concentrations, surfactant solutions self-assemble into lyotropic mesophases exhibiting complex rheology and viscoelasticity relevant for processing.[1, 2] These molecules can rearrange themselves depending on both chemical structure and the process. Furthermore, the microstructure of the system strongly affects the properties of the finished product, which are the determining factors for the specific application. It is, therefore, necessary to identify and study the chemical-physical processes that involve such systems. Industrial processing of surfactant-based materials typically includes a water dissolution step. It is well established that both physicochemical and rheological parameters, such as raw material chemistry, type of solvent, temperature and flow conditions, play a key role in the dissolution process[3]. However, the mechanisms governing the dissolution process are not well understood. This explains the great interest in the dissolution of complex molecules in flow or in static conditions. As a matter of fact, understanding the dissolution of the concentrated surfactant solutions in different solvents is of fundamental importance for their effective industrial application.

In this work video microscopy will be used to investigate dissolution in well-controlled static conditions, and the sample microstructure changes will be observed; a microfluidic device will be rearranged to evaluate the

effect of specific flow conditions with the aim to understand which is the controlling factor of the phenomenon and see differences from static results; in order to observe the process in a larger scale, a simple lab scale test will be set up and a Raman tool used to characterize the process in beaker with the aims to build a model to quantify the dissolution process and a correlation of this method with pilot plant scale test.

Introduction

I. Surfactants

Surfactants are molecules which have the ability to reduce the surface tension of a liquid, principally water, favoring surface wettability or miscibility with other liquids. Water molecules are joined together by various bonds, including hydrogen bonds. These strong bonds are responsible for the high surface tension of the water. Each water molecule present in the bulk is subject to isotropic attraction forces exerted by the other surrounding molecules. The resultant of these forces is, therefore, zero. On the other hand, molecules on the interface are not completely surrounded by similar ones and are more affected by their attractive forces that push the surface molecules towards the mass of the liquid. These forces contract the surface by varying the shape hindering the interface to increase. The surface tension is, therefore, a measure of the force with which the surface contracts. Surfactants reduce the surface tension of the water because the attraction forces between water-surfactant are lower than those between two hydrogen molecules and therefore the intensity of the contraction force of the interface is reduced[4].

Surfactants have high foaming, detergent, and solubilizing properties and it is for this reason that they are widely used in personal care and home care industry. They are also used in the production of paints, plastics, cosmetics and in the food industry, typically as stabilizers. Surfactants are organic compounds consisting of a hydrophilic head and a hydrophobic tail

typically containing from 8 to 18 carbon atoms. Molecules with these characteristics are defined more generally amphiphilic. The hydrophilic head interacts with polar solvents such as water by dipole-dipole or dipole-ion interactions. The hydrophobic tail, instead, tends to avoid water and to interact with non-polar molecules[5].

Surfactants have four levels of structures (complexity increases as a function of the structure).

1. Primary or molecular structure is based on the nature of the hydrophobic part; surfactants can be classified as:
    - *Anionic* – these are salts made of long chains of carbon atoms, with a negative charge group (e.g., an RCOO-M + carboxyl group, ROSO3-M + sulfate or RCPO3-M + phosphate). They are used for the production of detergents for washing machines and for hand washing; they are also used to obtain household cleaners and personal cleaning products. Linear sulfonated alkylbenzenes (LAS), ethoxy sulfate alcohols (AES), alkyl sulfates (AS) are the most common anionic surfactants. These are crystalline or amorphous solids. The linear sulfonated alkylbenzene (R-C6H4-SO3Na) is the one most widely used to obtain laundry products.
    - *Cationic* – for this, the positive part consists of long chains of carbon atoms ending in a quaternary amino group (R4N + X-). These surfactants are not used as detergents, as they are not good cleaning agents or good foaming agents. They are widely used in cosmetic products, such as hair conditioners. Cationic surfactants can cause irritation and

are incompatible with anionic surfactants with which they form insoluble salts in water. The best known cationic surfactants are benzalkonium chloride and cetyltrimethyl ammonium bromide.

- *Non-ionic* – these molecules do not have a net charge on the hydrophilic head, and polarity is due to the presence of atoms such as oxygen and nitrogen or ester and amide bonds. The salient characteristics of non-ionic surfactants are that they are insensitive to pH variations, have a certain foaming and thickening power. They are compatible with all other surfactants and are used in association with them. Non-ionic soaps, being characterized by a low level of aggression and a low probability of causing irritation and allergic problems, are widely used in cosmetic products for children.

- *Amphoters* – are electrically neutral molecules, which however have both negative and positive charges and behave as cationic or anionic surfactants respectively in an acid or alkaline environment. Some examples are coconut-amidopropyl-betaine, dodecyl-betaine, lecithin, and amino-carboxylic acids.

- *Polymeric* – block copolymers (diblock, triblock, endcapped). They are amphiphilic copolymers with some hydrophilic and hydrophobic parts.

2. Secondary or conformational structure, Thousands of conformations are possible in one surfactant molecule, for head group and tail; and this

affects packing between molecules. For the hydrophilic tail, the number of conformations that can exist is enormous:

Number of conformations = 3n, where n is the number of bonds.

3. Tertiary - phase structure, the manner in which molecules are arranged in space within a phase. What drives surfactant aggregations is:
    - Hydrophobic effect: strong H-bond between water molecules
    - Repulsive: hydrophobic interaction between water and hydrophobic alkyl chain (surface tension)
    - Attractive: Van Der Waals forces between hydrophobic alkyl chain (packing constraints) or head group interaction (head group of opposite charges)
    - Repulsive: head group interaction (ion-ion repulsion and steric interaction)
    - Head group solubility in water layer (repulsive or attractive depending on water quality)

    When surfactants are in solutions they concentrate on the surface due to their lyophilic and lyophobic groups, then a molecular aggregation happens. Liquid crystal formation is driven by temperature (thermotropic) or solvent dilution (lyotropic).

    - Anisotropic: birefringent.
    - Isotropic: appears dark under polarized light.
4. Quaternary or colloidal structure.

Characteristic of surfactants

Micellar critical concentration

Due to their amphiphilic nature, surfactant molecules arrange themselves in aqueous solution as monomers in bulk solution or monolayer along the

interface. As the surfactant concentration increases, saturation conditions are reached at the interface; the surfactant precipitates and tends to form molecular aggregates. At a critical concentration, called critical micellar concentration (CMC), the surfactant molecules spontaneously aggregate by physical interactions forming structures called micelles[6]

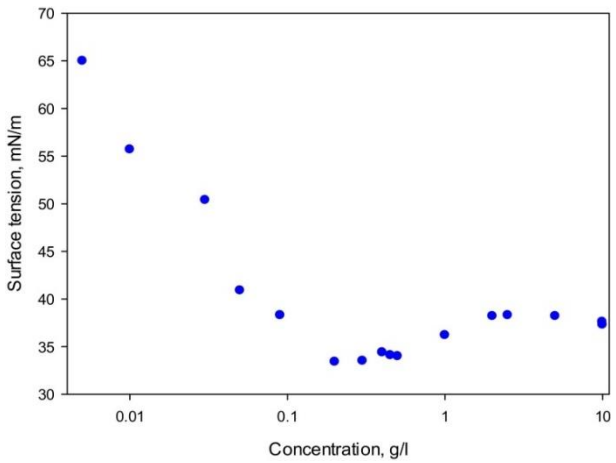

Figure 1 **Surface tension as function of SLES concentration[7]**

As shown in *Figure 1*, there is a sudden change in the slope to a particular concentration. At this concentration, some properties of a bulk solution such as surface tension, solubility, osmotic pressure, density, electrical resistance, turbidity, conductivity, show a change in their rate of variation with concentration. Light scattering experiments show that, at this critical concentration, micelles start to form.

In micellar form, the hydrocarbon chains are shielded from the water and the whole structure is hydrophilic and compatible with water. The CMC can be determined experimentally by measuring the surfactant concentration at which sudden changes in physical properties occur. Each surfactant has a specific value of CMC, in relation to the temperature and to the presence of solutes or co-solvents.

Surface active agent	*C.m.c. (mol dm^{-3})*
(A) Anionic	
Sodium octyl-l-sulphate	1.30×10^{-1}
Sodium decyl-l-sulphate	3.32×10^{-2}
Sodium dodecyl-l-sulphate	8.39×10^{-3}
Sodium tetradecyl-l-sulphate	2.05×10^{-3}
(B) Cationic	
Octyl trimethyl ammonium bromide	1.30×10^{-1}
Decetryl trimethyl ammonium bromide	6.46×10^{-2}
Dodecyl trimethyl ammonium bromide	1.56×10^{-2}
Hexacetyltrimethyl ammonium bromide	9.20×10^{-4}
(C) Nonionic	
Octyl hexaoxyethylene glycol monoether C_8E_6	9.80×10^{-3}
Decyl hexaoxyethylene glycol monoether $C_{10}E_6$	9.00×10^{-4}
Decyl nonaoxyethylene glycol monoether $C_{10}E_9$	1.30×10^{-3}
Dodecyl hexaoxyethylene glycol monoether $C_{12}E_6$	8.70×10^{-5}
Octylphenyl hexaoxyethylene glycol monoether C_8E_6	2.05×10^{-4}

***Figure 2* CMC for several kinds of surfactants.**

Non-ionic surfactants have very low CMC values, of the order of 10^{-5} mol/l; the anionic surfactants, on the other hand, have higher CMC values, of the order of 10^{-3} mol/l, since the electric repulsion of the charged head groups acts against the aggregation. In very diluted solutions, the micelles are not detectable. As the surfactant concentration increases, the size of the micelles aggregates increases. Beyond the micellar critical concentration, the interfacial properties do not change; for example, the surface tension remains almost constant beyond the CMC.

Temperatura di Krafft

Micellar aggregates are formed when the temperature is equal to or higher than the Krafft temperature. In fact, most of the anionic surfactants are highly soluble in water at high temperature; at low temperatures, however, such surfactants separate from the solution as a crystalline phase. The Krafft temperature represents the temperature at which the solubility becomes equal to the micellar concentration and therefore the formation of micelles is possible. The higher the temperature, the greater the solubility.

The following diagram shows the concentration against the temperature for an SDS surfactant in water. As we can see, the solubility strongly increases

following the formation of the micelles. The temperature of Krafft is exactly the intersection point between the curve of the CMC as a function of the temperature and the representative curve of the solubility limit.

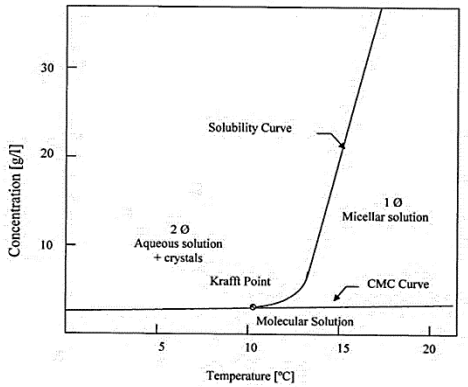

Figure 3 **CMC and solubility curves of SDS in water.**

Cloud point temperature

When a micellar solution of non-ionic surfactants is heated above a certain temperature value, called point of fog (cloud point), it becomes turbid. At this temperature, the micellar solution undergoes phase separation, obtaining a diluted solution whose concentration is equal to the micellar concentration at that temperature. Phase separation is reversible; when the mixture is cooled to temperatures below the cloud point, the two phases come together forming a new clear phase. The phase separation is believed to be due to the decrease in intermicellar repulsion and/or the sharp increase in the number of micelles. The value of the cloud point strongly depends on the chemical structure of the surfactant.

Hydrophile-Lipophile-Balance (HBL) and Phase Inversion Temperature (PIT)

A surfactant's hydrophile-lipophile balance is a measure of its degree of hydrophilicity or lipophilicity, determined by calculating it according to the

different regions of the molecule, as described by Griffin in 1949. Other methods have also been suggested, in particular in 1959 by Davies[6].

Griffin proposed the HLB parameter to define the characteristics of a surfactant. In particular, a non-ionic surfactant, theoretically 100% hydrophilic, is assigned the value of 20. Surfactants with HLB above 10 are hydrophilic and therefore tendentially soluble in water, whereas those with HLB lower than 10 are lipophilic and therefore tendentially soluble in oils

HLB defined by Griffin is

$$HLB = 20 * \frac{\mathrm{Mh}}{M} \quad (1)$$

Where Mh is just the molecular mass of the hydrophilic part while M is the molecular mass of the whole molecule. According to this formula, HBL has a value between 0 and 20, where 0 means completely lipophilic (Mh = 0), while an HLB of 20 means completely hydrophilic (Mh/M = 1).

In 1959, Davies suggested a new simple group method

$$HLB = 7 + m * Hh - n * Hl \quad (2)$$

where m is the number of hydrophilic groups in the molecule, Hh is the value of the hydrophilic groups, n is the number of lipophilic groups in the molecule, Hl is the value of the lipophilic groups.

HLB can be also used to know the surfactant properties of a molecule: anti-foam agent (HBL between 0 and 3), W/O emulsifier (4 – 6), humidifying (7 – 9), O/W emulsifier (8 – 18), or a hydrotrope (10 – 18) and finally a detergent (13 – 14).

Finally, especially for non-ionic surfactants, it is possible to define a phase inversion temperature (PIT), at which the surfactant turns from stabilizer for direct emulsions O / W into an O / W emulsifier or vice versa. According

to the phase rule, PIT is invariant at constant pressure in a three-component system but is also affected by the HLB.

Surfactants phase behavior characterization

Below the critical micelle concentration (CMC) surfactant molecules in the bulk liquid are “unstructured”. Once concentration exceeds the CMC, micelles start to form and the first isotropic phase micellar phase (L_1) appears. In non-ionic systems, at higher temperatures or concentrations and in the presence of hydrophobic organic solvents, there is an inverse micellar phase, indicated with L_2.

Both L_1 and L_2 can exist as a homogeneous phase or in equilibrium with the aqueous phase, depending on temperature and concentration.

As the surfactant concentration increases, the system undergoes the transition from an isotropic state of micellar aggregates to a crystalline liquid state characterized by a high structural order. The liquid structures that are formed are lipotropic, i.e. they depend on the concentration of surfactant and the interactions between the surfactant and solvent molecules. There are many types of mesophases; those generally associated with surfactants are: hexagonal (or middle phase), cubic, and lamellar (or neat phase).

Spherocylindrical micelles can arrange themselves in the hexagonal phase (H_1), or inverted hexagonal when 1 rod is surrounded by 6 rods (anisotropic). The middle phase has a high degree of micelle packing which is responsible for a high viscosity value. H_2 is the inverse hexagonal phase, formed of long, inverted cylindrical micelles aligned. Hexagonal phase can move freely only along their length (like uncooked spaghetti).

The cubic phase, referred to as V_1 (or V_2 for its inverted form), is another type of liquid crystalline phase. It presents spheroidal micelles packaged

according to a cubic model with centered body or centered faces. It is the most difficult to identify and the least known, characterized by the highest degree of viscosity. Although this phase is isotropic under crossed polarizers and therefore does not exhibit birefringences such as the hexagonal and lamellar phases, its microstructures can be examined by X-ray diffraction. Cubic phase has an interconnected structure with no shear planes.

The lamellar structure (Lα), is formed by double ordered layers of surfactant molecules alternated with water layers. In the lamellar phase, layers can slide with respect to each other favoring the flow and this determines a reduction in viscosity. The lamellar phase also shows static birefringence under crossed polarizers.

The liquid crystalline phases dissolve at sufficiently high temperatures in isotropic phases. Under crossed polarizers, the plot of different liquid crystalline phases looks very different. For example, the texture of the lamellar phase appears as a mosaic and focal conic, in contrast to a “marble-like” texture for the hexagonal phase.

Another isotropic phase, denoted as L3, is formed at temperatures higher than that in correspondence of which water and lamellar phases coexist. It is often called "sponge phase" because the continuous, but tortuous water channels, are separated by double surfactant layers, whose large-scale morphology resembles that of the solid part of a sponge. At the local level, the double layers are saddle-shaped with the two curving spokes with opposite signs. The main difference between the phases Lα and L_3 is that the initially flat bilayers of Lα are deformed in saddle-shaped surfaces in L_3.

Figure 4 shows the images under polarized light microscope in which it is possible to observe the hexagonal and lamellar phases. The isotropic microstructures, such as micellar, do not rotate the plane of polarized light and therefore in an optical microscope only a black region is observed.

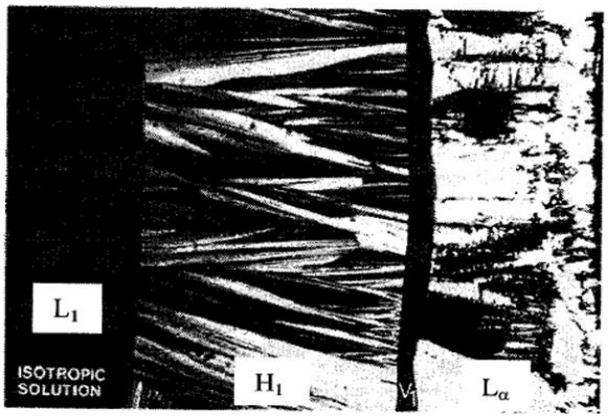

***Figure 4*: Optical properties of liquid crystals. Isotropic lamellar phase (L_1), hexagonal phase (H_1), cubic phase (V_1), lamellar phase (L_α)**

Figure 5 shows a typical phase diagram for a detergent-water system, in which the system states are represented as a function of the surfactant temperature and concentration. At room temperature and below the CMC, the surfactant molecules disperse as single molecules which, to minimize repulsive interactions with the solvent, tend to move to the interfaces. As the concentration increases, the molecules aggregate and form spherical micelles dispersed in the solution. Spherical micelles evolve towards worm-like structures and subsequently towards crystalline liquid phases for higher concentrations.

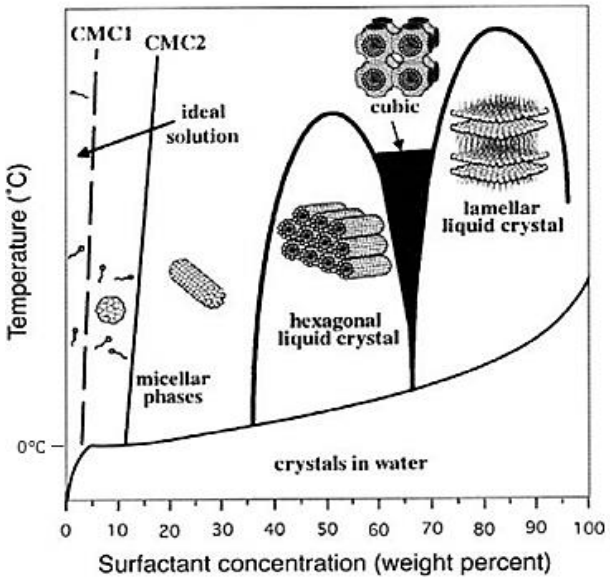

Figure 5: Classical surfactant in water phase diagram

Surfactants behave differently in solution depending on:

- Molecular structure
- Valency and type of counterion
- Concentration
- Temperature
- Pressure
- Presence of other water-soluble ingredients like electrolytes, polymers, co-surfactants, hydrotropes, co-solvents, oil, perfume and others

Phase behavior can affect product stability, physical and rheological properties, and even processability, dissolution profile, and performance.

Dissolution

Dissolution process of a complex fluid in a solvent is different between one fluid to another. In general, the process can be described according to the "diffusion layer" model, in which two stages are observed:

1. **Phase transition**, the complex fluid tends to dissolve at the interface with the dissolution medium. This involves the formation, at the interface, of a thin layer of a saturated solution called precisely diffusion layer.
2. **Diffusive transport**, in this case, the solute goes from the interface to the circulating solution (bulk). The solute molecules spread to the bulk solution, where the solute concentration is lower.

The dissolution speed is defined by the Noyes-Whitney law:

$$\frac{dc}{dt} = \mathrm{K} * \mathrm{S} * (\mathrm{C}_S - C_T) \qquad (3)$$

where:

- $\frac{dc}{dt}$ is the dissolution rate, i.e. the variation of solute concentration in the unit of time;
- K is a constant;
- S is the specific surface of the particles (area per unit of volume);
- C_S is the concentration in the diffusion layer, i.e. the solubility of the substance;
- C_T is the concentration in the surrounding solvent (bulk solution) at a certain time t

Actually, (C_S–C_T) is the concentration gradient.

From equation (3) the main factors that influence the dissolution process are:

- ***Specific surface***, the ratio between the area and the volume of the particles (it increases as the size of the part-cell decreases);
- ***Solubility***, which corresponds to the maximum concentration of a solute in a known amount of solvent at a given temperature;
- ***Diffusion coefficient***, which rules the amount of solute that diffuses through the diffusion layer.

The diffusion coefficient depends on:

- solute molecular mass (the greater the size of the molecule, the greater the diffusion coefficient);
- solute concentration;
- solvent viscosity (the higher the viscosity of the solvent, the lower the diffusion coefficient, since the flow between the solvent and solute molecules is slowed down);
- temperature (the higher the temperature, the greater the diffusion coefficient, since it increases the kinetic energy and therefore the mobility of the solute molecules).

Other factors like system temperature, solute and solvent' s characteristic and properties (like viscosity and PH)

Kinetic of surfactants dissolution

Surfactants dissolution is of fundamental importance in many industrial and scientific applications. Even today dissolution is not well known.

When a surfactant goes in contact with water, there is an inter-diffusion of the two molecular species, accompanied by the formation of mesophases, at the solvent/surfactant interface, which influences the evolution of the system during the dissolution process [8]. The simple growth of the mesophases could, in fact, lead to considerable instability

In order to fully understand the phenomenon of dissolution, one must have a good knowledge of the behavior of the equilibrium system.

Mostly, surfactants dissolution is diffusion limited; this means that, at any point in the system, the observed mesophase corresponds to the expected equilibrium phase based on the local composition. At the interface, there are several intermediate steps and the relative rapidity with which these mesophases are formed is the reason why the dissolution of a surfactant tends to be controlled by diffusion. The transition time from one phase to another, in fact, is typically one second or less. Mesophases appear quickly because molecules have to spread over very small distances ($\lambda \sim 10$nm) to assemble into a new structure and give life to a new phase. An estimate of the diffusion time is given by $\lambda^2/D = 1$ μs (or ms)[9]. Experimentally, therefore, it is difficult to observe the initial stages of the dissolution process because just a minimal amount of the new phase is formed at this time.

Two are the diffusive processes involved in dissolution:

- self-diffusion, molecules move individually;
- collective diffusion, which is the response of a given species to a concentration gradient (which can be generated by another species).

In a solvent/surfactant solution, there are two self-diffusion coefficients (one for the surfactant and another for the solvent) and a single coefficient

of collective diffusion since a concentration gradient for the surfactant inevitably implies a concentration gradient for the solvent. It is better to underline that the collective diffusion coefficient is important in the dissolution processes of surfactants.

The self-diffusion coefficient for a molecular species is defined as the rate of growth over time of the average displacement of the squared molecules. Typically, the values are of the order of 10^{-12} - 10^{-11} m^2/s for the surfactant molecules in a mesophase. The upper limit is representative of the diffusion coefficient of a surfactant in a micellar solution. The self-diffusion coefficient of a solvent is usually of an order of magnitude smaller than the self-diffusion coefficient of the same solvent considered as pure. This reduction can be attributed to the obstacles to the dissolution of the solvent represented by the surfactant structure. Collective diffusion coefficients can be measured by dynamic light scattering (DLS) experiments.

In an experiment of surfactant dissolution, what is observed most frequently is that the interface between the phases remains clear and the mesophases remain homogeneous. In some cases, however, dramatic instability can occur. The myeline is an example of interfacial instability still little known, which manifests itself during the swelling of a lamellar phase of surfactant in an aqueous phase (provided that the lamellas are themselves long-lived). The myeline can be schematized as multi lamellar tubules, typically having a length of a few tens of microns. They grow during swelling and may have different structures depending on the growth time[9].

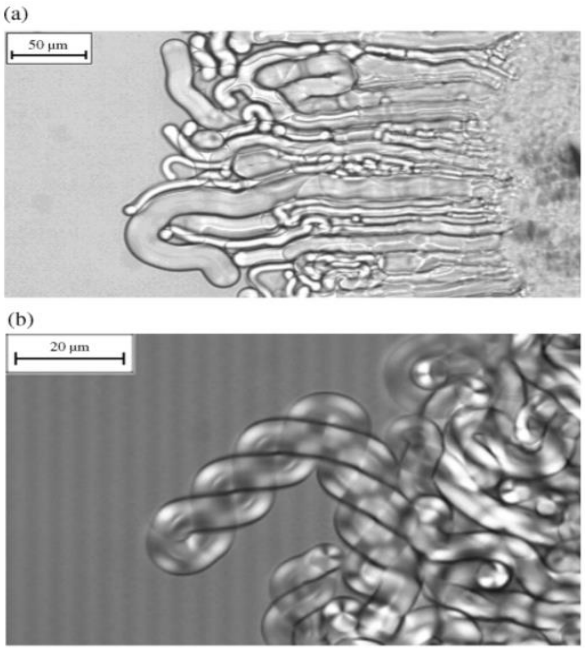

***Figure 6*: structure of the mielines at the interface for a solvent/surfactant system at different times**

The swelling that occurs and that could lead to the emergence of these instabilities can, in some way, recall an analogy with the swelling that occurs in complex systems, such as glass polymers.

When a glass polymer is put into contact with a thermodynamically compatible solvent, the solvent diffuses into the polymer[10]. Due to the more "plastic" nature of the polymer with respect to the solvent, a gel-like swelling layer is formed which creates two separate interfaces, one between the glass polymer and the gel layer and the other between the gel layer and the gel layer. solvent. In the initial phase, therefore, a swelling can be observed. After a certain period, called "induction time", the polymer begins to dissolve. However, there are also cases in which cracks are formed and no gel layer is formed.

The process involves an initial aggression of the solvent on the polymer, which tends to penetrate into it; with the passage of time, a more diluted upper layer of the polymer is pushed in the direction of the solvent flow. The penetration of the solvent into the solid polymer, which gradually increases the swelling of the surface layer, ends when an almost-stationary state is reached, in which the transport of the macromolecules from the surface into the solution prevents a further increase in the level. This phase corresponds to the end of the swelling time.

Obviously, this swelling that in the case of glass polymers takes place in very long times, in the case of surfactants it manifests itself on very small timescales, lower than the second.

II. Sodium Lauryl Ether 3 Sulfate

Sodium Laureth sulfate (SLES), an accepted contraction of sodium lauryl ether sulfate (SLES), is an anionic detergent and surfactant found in many categories of detergent products (soaps, shampoos, toothpaste etc.). SLES is an inexpensive and very effective foaming agent. SLES, as well as sodium lauryl sulfate (SLS), ammonium lauryl sulfate (ALS), and sodium Laureth sulfate is also used in many cosmetic products for its cleaning and emulsifying properties.

SLES is prepared by ethoxylation of dodecyl alcohol. The resulting ethoxylate is converted to a half ester of sulfuric acid, which is neutralized by conversion to the sodium salt. The related surfactant sodium lauryl sulfate (also known as sodium dodecyl sulfate or SDS) is produced similarly, but without the ethoxylation step. SLS and ammonium lauryl sulfate (ALS) are commonly used alternatives to SLES in consumer products[11]

Its chemical formula is $CH_3(CH_2)_{11}(OCH_2CH_2)_nOSO_3Na$. Sometimes the number represented by n is specified in the name, e.g. Laureth-2 sulfate. The product is heterogeneous in the number of ethoxy groups, where n is the mean. It is common for commercial products for n= 3.

The hydrophilic head comprises three ether groups and a charged $(SO_3)^-$ group at the end with a sodium counterion, and its structure is similar to the ubiquitous Sodium Dodecyl Sulphate (SDS) surfactant except for the three extra ether groups[1].

When diluted with water, SLES shows gel structures which are typical of ether sulfates. After the addition of water, the viscosity first increases rather

rapidly, and after a reduction of the active substance to a level below 30 %, it decreases considerably. Liquid, stable solutions are obtained up to 28 % of the active substance. At higher concentrations the product becomes pasty.

SLES has an extremely low salt content, and when diluted with water to the normal use concentration, it shows a very low viscosity. When sodium chloride and alkanolamides are added, the viscosity can be adjusted accordingly. In this way, the viscosity of diluted solutions of SLES 70 with approx. 5 - 28 % washing-active substance can be easily increased to the desired value.

Alkyl ethoxy sulphates (AES), like SLES, together with linear alkylbenzenesulfonate (LAS) is commonly used as commercial anionic surfactant, as major components of laundry detergent and is widely used in many household cleaning detergents, personal care, and consumer products. AES and LAS are often used together in the process of producing detergent, which makes the investigation of this system of great importance. However, amphiphilic molecules of surfactant are prone to self-assemble into many morphologies in water, mainly including micelle phase and liquid crystalline phases, such as hexagonal, lamellar, and cubic phases[12, 13], which exhibit complex phase behavior. Among these phases, the hexagonal and cubic phases are very viscous, which limits their application[14, 15]. Lamellar phase and some mesophases have shown relatively lower viscosity and have found application in several studies[16, 17]. Therefore, it is necessary to reduce the viscosity of hexagonal and cubic phases during production or find methods to transform the hexagonal phase and bicontinuous cubic phases into the low-viscosity lamellar and mesophases[3].

LAS/AES/H_2O phase diagram

In a previous study[3], polarizing microscope and small-angle X-ray scattering were performed to determine phases. Since liquid crystals in different phases have different polarized optical textures, they can be identified with a polarizing microscope. Furthermore, the small-angle X-ray scattering method was used to confirm the former result. Rheological measurements were also used to investigate the viscosity distribution and rheological behavior of this system. In particular, the phase behavior of the LAS/AES/H2O system has been examined by preparing samples over the whole composition range of the ternary phase diagram. The composition interval was selected as 5% for a rough mapping and the smaller intervals of 2% were chosen to define the phase boundaries in the region of phase transitions. Phase equilibrium was determined by visual observation.

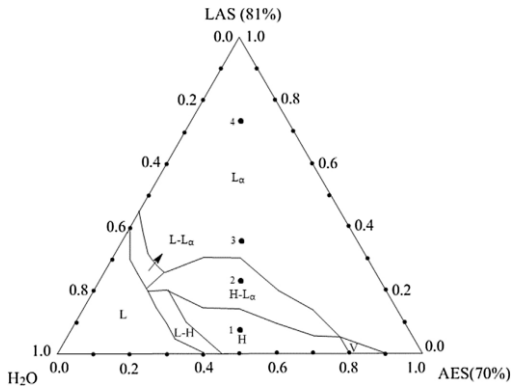

Figure 7 **Phase diagram of LAS/AES/H_2O system at 25°C.**

Observing the phase diagram along the AES/H2O binary axis, four different phases were observed: a lamellar phase (Lα) from the raw paste 70% down to 63 wt.%; a cubic phase (V) from 63% to 56%; hexagonal phase (H) from 56% to 31.5%, micellar phase (L) from 28% to CMC (0.0236 %) and one multiphase: L-H, during the phase transition from H to L.

III. Aim of this work

This work has the object to investigate and understand the dissolution process of SLES and find the controlling factor with the aim to make the process predictable and finally optimize it.

In order to approach to the study of dissolution, different scale tests will be carried out, starting from simple static conditions, to well-controlled microfluidic flow, medium size lab-scale apparatus, up to pilot plant experimental campaigns.

This thesis will be organized in chapters that are based on under submission or under preparation papers.

- In the first chapter will be reported the results of a preliminary study, carried out in collaboration with other two research groups, proposing a multi-technique approach to investigate the dissolution process, going through a rheological characterization of the system that shows non-monotonic changes of several orders of magnitude in its viscosity as a function of water content; observation of phase changes' evolution as water penetrates in a disk-shaped sample by time-lapse microscopy and digital image analysis; finally a multi-parameter diffusive model, whose parameter values well fit the rheological and microscopy data. The results of this preliminary work lead to a first paper, that will be submitted to Chemical Engineering Journal.

- Afterward, in order to investigate the interaction between surfactant and water, a systematic experimental investigation of single paste droplets dissolution in static conditions will be performed. Differences between phases were highlighted using conoscopy image technique, and a dynamic rearrangement in the sample texture over time will be observed and

quantified using microbeads. These results will be reported in chapter 2 and summarised in a paper that will be submitted to Langmuir.

- Subsequently, a home-made microfluidic device will be used to apply a well-controlled flow to the disc-shaped paste and, by time-lapse microscopy, dissolution time will be quantified. Firstly, different flow conditions will be tested using only pure water as a solvent, then, in order to modify the physical, chemical or rheological properties of the system, different solvents will be used, trying to understand the effect of chemical and mechanical stress on the process.

- Subsequently, a medium scale experimental setup will be developed, this will be easier to use but also will be used to build a correlation between the results obtained with the microfluidic setup and tests that will be carried out in the pilot plant. To do this, a certain amount of SLES will be dissolved in a beaker using a blade agitator, testing the effect of stirring speed and concentration gradient. The dissolution process, in several conditions tested, will be monitored by measuring the value of the conductivity of the solution or of the Raman signal (both measured by means of probes that can be inserted directly in solution). From the fitting of the experimental data, a characteristic dissolution time will be extrapolated, specific for each speed and concentration condition.

- Finally, a pilot plant scale set-up will be developed at the Procter & Gamble research center in Beijing. The operating conditions in which the tests will be carried out, similar to those used in the laboratory, and set up details will be described in chapter 4. As well as for the lab tests, from the experimental campaign conducted in the pilot plant, characteristic dissolution times for each various conditions will be taken out and these will be compared with the results obtained in the laboratory scale.

- The last chapter summarizes the current findings of this work and draws directions for future works and applications.

CHAPTER 1

Dissolution of concentrated surfactant solutions: from microscopy imaging to rheological measurements through numerical simulations.

Discussions contained in this chapter are under submission within: Rosa Ilaria Castaldo[†], Rossana Pasquino[†], Massimiliano M. Villone[†], Sergio Caserta, Chong Gu, Nino Grizzuti, Stefano Guido, Pier Luca Maffettone, Vincenzo Guida. *Dissolution of concentrated surfactant solutions: from microscopy imaging to rheological measurements through numerical simulations*. Chemical Engineering Journal.

1.1 Abstract

Many surfactants used in detergents experience complex phase and rheology changes when a thick paste is dissolved in water. During the dilution process, depending on water content, surfactant molecules can arrange in different morphologies, such as lamellas or cubic and hexagonal structures. These phases are characterized by different physicochemical properties, such as viscosity or diffusivity, which lead to non-simple transport mechanisms during the dissolution process.

In this work, we propose a multi-technique approach to investigate the dissolution of concentrated Sodium Lauryl Ether Sulfate (SLES) pastes in water under static and flow conditions. A thorough rheological characterization of the system showed non-monotonic changes of several orders of magnitude in its viscosity and viscoelastic moduli as a function of water content. Time-lapse microscopy allowed to image the dynamic evolution of the phase changes as water penetrated in a disk-shaped sample (with the same a geometry used in rheological tests). A simple diffusion-based multi-parameter model can describe satisfactorily both static and dynamic SLES dissolution data.

1.2 Introduction

SURFace ACTive AgeNTS (Surfactants) are molecules which have the ability to reduce the surface tension between a liquid, typically water, and another phase, favoring surface wettability, and miscibility with other liquids. They have high foaming, detergent, and solubilizing properties and it is for this reason that they are widely used in the personal-, home-, and beauty-care industry. Detergents and cosmetics are typically surfactant aqueous solutions18.

The industrial process for the preparation of commercial products typically involves mixing and dilution of originally highly concentrated surfactant pastes. At high concentration, surfactant molecules self-assemble into lyotropic mesophases exhibiting complex microstructure and rheology that are relevant for industrial processing1, 2. As concentration changes, molecules can rearrange, thus changing the microstructure of the system that in turn strongly affects the properties of the final product, which are determinant for its specific application. Therefore, it is necessary to identify and study the physicochemical processes involved in such transformations.

Industrial processing of surfactant-based materials typically includes a water-dissolution step.

The dissolution of surfactant pastes presents some similarities with the polymer dissolution19, 20 but is made more difficult by the following aspects: 1) surfactant monomers form aggregates of variable size and shape that can vary with dilution and can dynamically form and disintegrate 2) the surfactant paste already contains the solvent (i.e. water), which makes the diffusion process "reversible" and more complex 3) the diffusion coefficient can be dependent in a non-monotonic way on the surfactant concentration, giving rise to multiple interfaces, difficult to be predicted.

When a surfactant comes in contact with water, there is an inter-diffusion of the two molecular species, accompanied by the formation of mesophases9, which influence the evolution of the system during the dissolution process8, 21. It is well established that both physicochemical and rheological parameters, such as raw material chemistry, type of solvent, temperature and flow conditions, play a key role in the dissolution process3. However, the mechanisms governing the dissolution process are still not completely understood22, 23. This explains the great interest in the study

of the dissolution of complex molecules under static conditions and in flow2, 24-27, Understanding the dissolution of concentrated surfactant solutions in different solvents is of fundamental importance for their effective and wide industrial application.

The dissolution of surfactants in a solvent is diffusion-limited and, in general, can be described according to the diffusion layer model, in which two stages are observed: phase transition and diffusive transport. In order to fully understand the phenomenon of dissolution, then, one must have a good knowledge of the behavior of the equilibrium system. The equilibrium phase behavior of surfactant solutions has been extensively studied for different amphiphilic molecules and solvents28-30.

In this study, we consider Sodium Lauryl Ether Sulfate (SLES) as a model system. SLES is an anionic surfactant found in many categories of detergent products, e.g., soap, shampoo, and toothpaste, for its cheapness and effective foaming capacity. Recently, Poulos et al.1 have studied the dissolution of concentrate SLES in quiescent water through polarized light optical microscopy in both linear and circular geometries, finding bands with sharp interfaces. Their optical textures relate to cubic, hexagonal, and micellar phases appearing during the dilution of the concentrated surfactant. By tracking the movement of such bands, they have shown that dissolution can be modeled as a diffusive process and that it is possible to extract effective diffusion coefficients for each phase. In this work, we propose a multi-technique approach to investigate the SLES dissolution process both in static and flow conditions. We carry out a rheological characterization of the system in steady and oscillatory shear flow, a time-lapse-microscopy observation of phase-change evolution as water penetrates in a disk-shaped sample under static conditions, and finally we rationalize the two experimental contributions by a multi-parameter diffusive model, whose

parameter values give a satisfactory fit of both the rheological and microscopy data. To the best of our knowledge, static and dynamic dissolution experiments are here combined and rationalized under a unique framework for the first time.

1.3 Materials and methods

The surfactant used in our test is an Alkyl Ethoxy Sulphate (AES) paste provided by Procter and Gamble (Beijing, China). In particular, we will consider Sodium Lauryl Ether Sulfate (SLES, also known with its contract name Sodium Laureth 3 Sulfate, molecular weight = 288.38 g/mol31). A SLES concentrated paste 70%wt in water (density = 1.05 g/cm3 31) was available, and used without further purification. It is known that SLES in water can have a complex phase diagram, showing different morphologies. In particular, a Lamellar (Lα, 70-63%wt), Cubic (V1, 63-56%wt), Hexagonal (H, 56-31.5%wt) and Micellar phase (L1, 28-0.0236%wt) can be observed as a function of the concentration3. In the range 31.5-28%wt there is the coexistence of L1-H phases.

Aqueous solutions containing SLES ad different concentrations in the range 15-70%wt were prepared by adding the right amount of bi-distilled water to the concentrated raw paste. Equilibrium properties were reached by mixing samples with a magnetic stirrer for few days and continuous rheological tests were performed to prove stability over time.

Rheological setup

Rheological experiments were made with a stress-controlled rheometer (Physica, Anton Paar MCR702) equipped with a plate-plate geometry. In particular, frequency sweeps were performed at different concentrations in

the frequency range 100-0.1 rad/s in the linear regime (previously evaluated via strain sweep experiments). Flow curves were measured by tuning the shear rate in the range 100-0.01 s^{-1} by decreasing the sampling time at increasing shear rate.

The dissolution process was studied via a home-made plate-plate apparatus consisting of a water reservoir surrounding the surfactant paste mounted on a classical stress-controlled rheometer (Physica, Anton Paar MCR702), shown in *Figure 8a*. The raw paste was loaded between the rheometer plates, at time t = 0 water was added to the reservoir until reaching the total height of the plate-plate geometry (see schematic drawing in *Figure 8a*). A dynamic test at fixed frequency of 1 rad/s and low strain of 0.1% was performed at room temperature. The plate-plate gap was kept constant during the entire test. Two different plate-plate gaps (of 1 and 0.1 mm) and two different plate diameters (of 8 and 25 mm) were used in the experiments. During the dissolution process, the torque was monitored over time with the aim to relate its evolution to the morphological transitions arising in the sample.

Optical setup

Time-lapse microscopy was used to investigate SLES dissolution in water under static conditions. A microscope (Zeiss Axiovert 200, 10x and 20x objectives) was equipped with a high sensitivity CCD camera (Hamamatsu OrcaAG) and motorized stage, controlled by a home-made software, for automatic mosaic scanning of large samples[32]. The observation was done using two crossed polarizers, in order to visualize the internal microstructure. A tiny amount of raw surfactant paste (≈ 4 mg) was squeezed between the bottom glass of a home-made rectangular glass

chamber (12.5x8.5x2 cm) and a coverslip, obtaining a disk-shaped sample with an initial radius of about 4 mm. Sample thickness was set by inserting a double-side adhesive tape as a spacer between the two glass surfaces and measured to be 100 μm. A fixed amount of water (15 ml) was added in the surrounding chamber at time t = 0 in order to induce sample dissolution. Experiments were run at room temperature (≈ 25°C). In *Figure 8b*, a sketch of the experimental setup is reported.

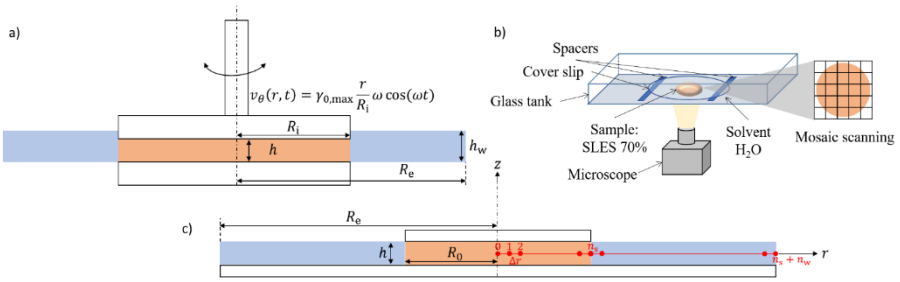

Figure 8 **(Not to scale) schematic drawings of the rheological setup (a), the optical setup (b), and of the computational domain for static dissolution numerical simulation (c).**

Numerical model

In order to reproduce the experimental setup shown in *Figure 8b*, we considered a disk of 70%wt surfactant paste of initial radius R_0 = 4 mm and thickness h = 1 mm surrounded by a coaxial "cage" of (initially pure) water with radius R_e = 24 mm. A (not to scale) schematic drawing of such system is given in *Figure 8c*.

Given the axial symmetry and the absence of fluid convective motion, the system can be modeled by the transient mass balance equation on the surfactant in 1D along the radial direction. Assuming that the Fickian constitutive equation holds for the surfactant diffusion, the balance equation reads

$$\frac{\partial c}{\partial t} = \frac{1}{r}\frac{\partial}{\partial r}\left[rD\frac{\partial c}{\partial r}\right] \quad (1)$$

where t is the time, r is the radial coordinate, c = c(r,t) is the (time- and position-dependent) surfactant molar concentration, and D = D(c) is the concentration-dependent diffusion coefficient of the surfactant. Expansion of Eq. 1 yields

$$\frac{\partial c}{\partial t} = \frac{\partial D}{\partial r}\frac{\partial c}{\partial r} + \frac{D}{r}\frac{\partial c}{\partial r} + D\frac{\partial^2 c}{\partial r^2} \quad (2)$$

The model is supplied with the Boundary Conditions (BC)

$$\left.\frac{\partial c}{\partial r}\right|_{r=0} = 0 \quad (3)$$

$$c|_{r=R_e} = 0 \quad (4)$$

and the Initial Condition (IC)

$$c|_{t=0} = \begin{cases} c_0 \ \forall r \in [0, R_0] \\ 0 \ \forall r \in]R_0, R_e] \end{cases} \quad (5)$$

Equation 3 expresses the axial symmetry at r = 0, whereas Eq. 4 gives the condition at r = R_e. Strictly speaking, this would be valid at $r \to \infty$, but we assumed it holds since R_e >> R_0 (and we verified it as explained in the following). Finally, Eq. 5 is the initial condition on the whole domain, with the surfactant concentration being c_0 = 0.7/MW (where MW is the surfactant molecular weight) inside the disk and 0 outside.

In order to solve Eq. 2 with BCs 3-4 and IC 5, we discretized the domain into $n_s + n_w$ intervals of length Δr (bounded by n_s + nw + 1 nodes) as shown in *Figure 8c*, then we discretized Eq. 2 through the Finite Difference Method[33]. By choosing a second-order centered scheme for spatial

derivatives, from node 1 to node $n_s + n_w - 1$ the discretized mass balance equation reads

$$\frac{\partial c_i}{\partial t} = \frac{D_{i-1}}{4\Delta r^2}(c_{i-1} - c_{i+1}) + \frac{D_{i+1}}{4\Delta r^2}(c_{i+1} - c_{i-1}) + \frac{D_i}{2i\Delta r^2}[(2i+1)c_{i+1} - 4ic_i + (2i-1)c_{i-1}] \quad (6)$$

In node 0, the discretized Neumann BC reads

$$\frac{\partial c_0}{\partial t} = \frac{4D_0}{\Delta r^2}(c_1 - c_0) \quad (7)$$

whereas in node $n_s + n_w$ we have the Dirichlet BC

$$c_{n_s+n_w} = 0 \quad (8)$$

At time 0, we imposed

$$c_i = \begin{cases} c_0 \ \forall i = 0, \dots n_s \\ 0 \ \forall i = n_s + 1, \dots, n_s + n_w \end{cases} \quad (9)$$

Notice that in Eq. 6 also the diffusion coefficient D appears with a subscript, because, since we considered a dependence of such parameter on the surfactant concentration, in each node the D_i-value depends on the c_i-value. In order to model this dependence, we assumed that each surfactant morphological phase is characterized by a specific value of the diffusion coefficient and that such value is constant for every concentration in that phase. In other words, in each node D_i could attain one out of four different values, depending on the phase (lamellar, hexagonal, cubic, or micellar) assumed by the surfactant.

Based on the above-mentioned assumptions, the model constituted by Eqs. 6-9 could be solved once the values of the three critical concentrations for phase transitions and of the four diffusion coefficients were chosen, yielding the numerically simulated time-varying radial profile of the

surfactant concentration in the domain shown in *Figure 8c*. From this, the numerical temporal trends of the radial positions of the three phase-transition fronts could be obtained. Such trends are shown and discussed below. We remark that preliminary space- and time-convergence test were performed, i.e., space- and time-discretization for the solution of Eqs. 6-9 were chosen as to ensure invariance of the numerical results upon further refinements, and that the water cage was large enough so that the condition imposed through Eq. 8 had no influence on the front displacements.

1.4 Results

Sample characterization

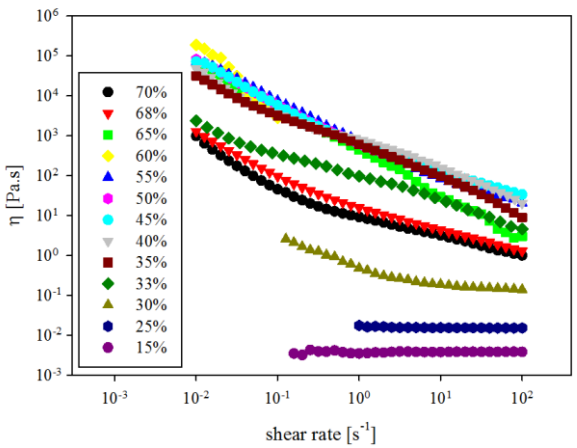

Figure 9 **Viscosity curves for various SLES concentrations (see legend for details).**

In *Figure 9*, steady viscosity data as a function of the shear rate are shown, parametric in SLES concentration. A Newtonian behavior is recorded when the surfactant concentration is low. As its concentration increases, the viscosity increases too and a shear thinning behavior can always be recorded, with the appearance in some cases of a yield stress. In addition, it

is apparent from *Figure 9* that the viscosity increase at increasing SLES concentration is not monotonic.

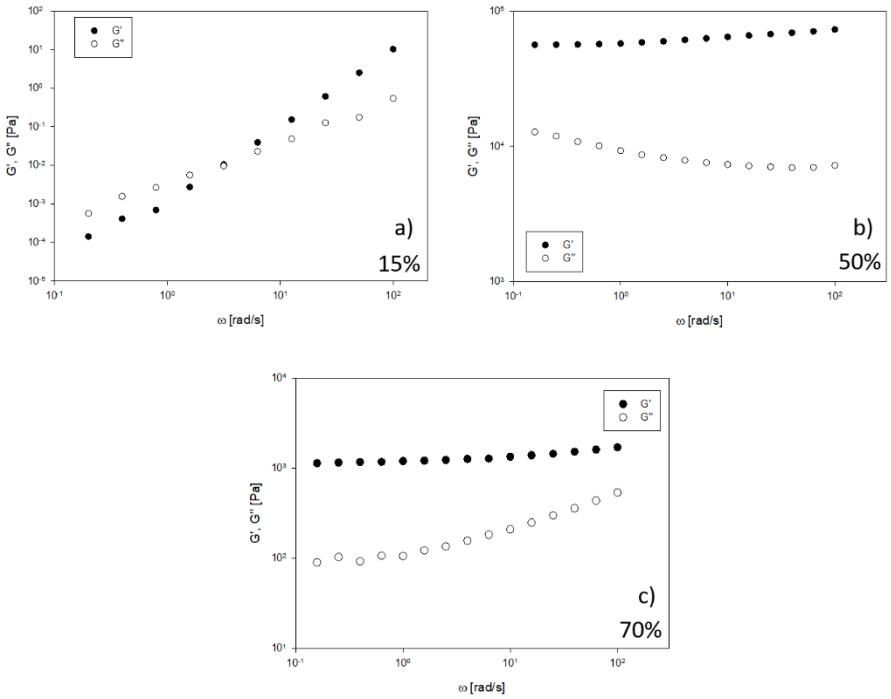

Figure 10 **Viscoelastic moduli as function of angular frequency for 15%wt (a), 50%wt (b) and 70%wt (c) SLES.**

Figure 10 shows the linear viscoelastic envelopes on samples containing different SLES amounts. By tuning the concentration, it is possible to induce morphological transitions that, in turn, influence the rheological response. The most concentrated sample (70%wt) shows the peculiar response of a soft-solid-like material, with the elastic modulus overcoming the viscous one in the whole frequency range (see *Figure 10c*). A similar viscoelastic behavior is reported in Figure 10b for the 50%wt sample. Although counterintuitive, higher moduli than for the concentrated sample are recorded. On the other hand, the less concentrated sample (30%wt, see *Figure 10a*) shows the typical response of a viscoelastic fluid, with a well-

defined cross-over frequency, which can be easily translated into a characteristic time for the micellar structure.

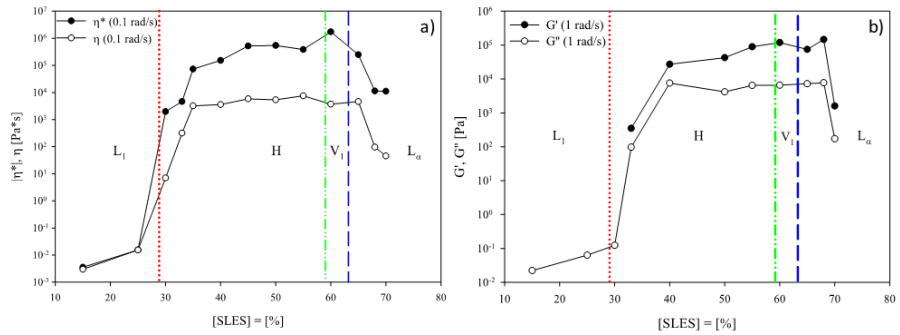

Figure 11 **a) Magnitude of the complex viscosity at a frequency of 1 rad/s (black circles) and steady viscosity at a shear rate of $1s^{-1}$ (white circles) as a function of SLES concentration. b) Elastic modulus (black circles) and loss modulus (white circles) at a frequency of 1 rad/s as a function of SLES concentration. The dashed lines represent morphological transitions: L_1 micellar phase, H hexagonal phase, V_1 cubic phase, L_a lamellar phase.**

In order to understand how the rheological response of the sample depends on SLES concentration, i.e. what is the relation between structure and rheology, and also to verify the applicability of the Cox-Merz rule, *Figure 11* reports the overlay between the magnitude of the complex viscosity and the steady viscosity at a specific angular frequency/shear rate (panel a) and the viscoelastic moduli at a specific angular frequency (panel b) as function of the SLES concentration. Morphological transitions, whose values have been identified by vertical lines, according to the thermodynamic phase diagram[3], have been marked with vertical dashed lines and different letters have been used to label the incoming microstructures (see legend for details). Some information arises from *Figure 11*: (i) it is actually possible to detect phase transitions via rheological methods, (ii) rheological parameters are non-monotonic with SLES concentration: the maxima correspond to cubic and hexagonal phases, whereas the lower levels of viscosity and moduli are related to the micellar phase, (iii) the Cox-Merz rule is not valid (as expected), except for the micellar phase; the magnitude

of the complex viscosity, which depicts equilibrium properties, is always higher than the steady viscosity, as flow can strongly influence the sample microstructure, (iv) except for L_1, all the other morphologies show a pronounced elastic response.

Optical experiments

In this section, we report the results of the time-lapse microscopy analysis of the dissolution process made using the optical experimental setup described above. After adding water into the chamber (at t = 0), the surfactant paste that is confined between the two glass surfaces (see *Figure 8b*) came in touch with the solvent and started to dissolve. Water penetrated radially changing the sample concentration and its microstructure. In *Figure 12*, we report on the left a mosaic scanning of the entire disk paste acquired in polarized light during the dissolution process. On the right, a zoom of a radial section of the same image is reported. The sample shows an onion-like radially layered structure and it is possible to identify four different regions, in agreement with the SLES phase diagram. A L_α core is surrounded by two concentric shells (V_1 and H), while the external phase is a micellar solution (L_1) that appears completely black because it is not birefringent. The boundaries between the phases are clearly visible and highlighted with different lines in the zoom on the right: the blue dashed line separates the lamellar core from the cubic layer (L_α-V_1), the green dash-double-dot line identifies the boundary between the cubic layer and the hexagonal shell (V_1-H), finally the red dotted line identifies the external boundary between the hexagonal and the micellar phase (H-L_1). The line-color code is in agreement with the rheological phase diagram reported in *Figure 11*.

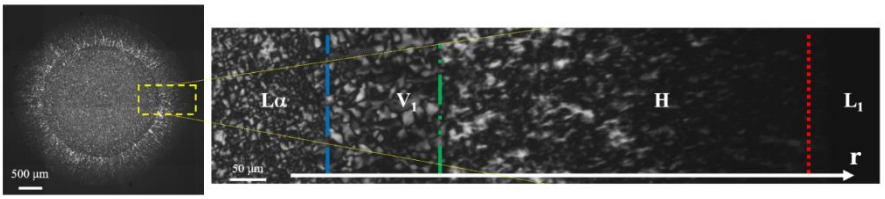

Figure 12 **Optical experiments. During the dissolution of a surfactant disk, it is possible to visualize 4 different phases: an internal core of lamellar phase ($L_{\square}$), a first ring of cubic phase (V_1), a second ring of hexagonal phase (H), and a more external micellar phase (L_1). The interfaces between the phases shrink radially as dissolution goes on.**

The time evolution of interface positions was measured by image analysis techniques. As time passed, the three boundaries shrank toward the center of the sample, so that at the end of the experiment the surfactant paste was dissolved, leaving only a black micellar solution. During the experiment, the distances of the interfaces from the center of the surfactant disk were manually identified. In *Figure 13*, the radial displacement of the 3 fronts is reported as a function of time. Red dots, up green triangles and down blue triangles identify the H-L_1, V_1-H, and L_α-V_1 transition, respectively. As the dissolution process went on, the radial position of the interfaces decreased down to zero, when the inner phase disappears. It is evident that the time evolutions of the two "internal" interfaces (L_α-V_1 and V_1-H) are "faster" than the external interface (H-L_1). This means that the entire process is controlled by the "slow" external transition between the hexagonal and the micellar phase. In our experimental conditions, when the lamellar and cubic phases had disappeared, the hexagonal phase sample was still about half of its original size.

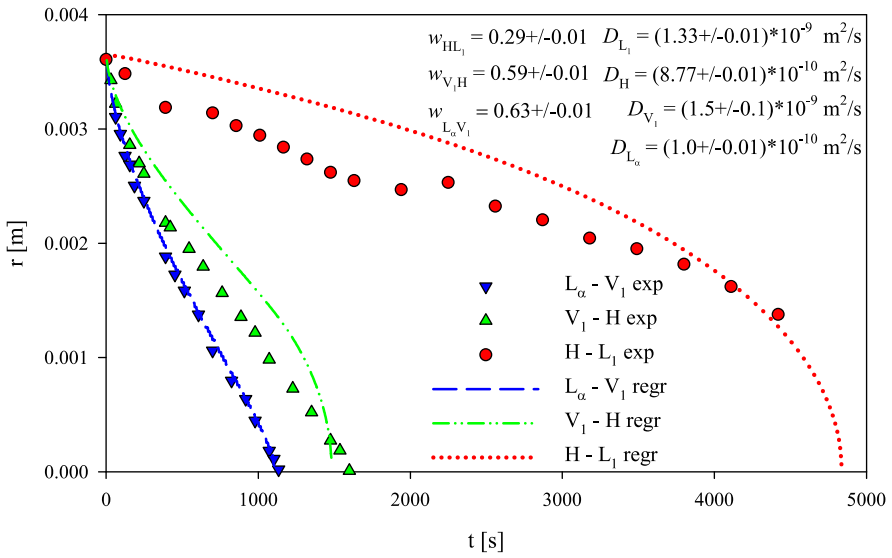

Figure 13 **Radial displacements of the L_a-V_1, V_1-H, and H-L_1 phase-transition fronts during the dissolution of a 4-mm-radius 70%wt surfactant disk. Symbols: experimental measurements; Curves: Least Squares fits by a Fickian diffusion model (the estimated parameters reported in the legend).**

Experimental data fit

In order to find the values of the phase-transition concentrations and of the diffusion coefficients yielding the experimentally measured front displacements reported in *Figure 12* (and to validate the simple model based on Fickian diffusion depicted above), we performed a fit of the experimental data in *Figure 13* based on the model presented in Sec. 2. In order to do that, as there is no analytical expression for the front displacements as a function of the parameters, we applied an iterative procedure, namely, we numerically solved the linear system given by Eqs. 6-9 repeatedly at varying the values of the 7 parameters in appropriate ranges, then we "selected" the parameter set for which the sum of the squared differences between the experimental and the numerical data was the minimum. The ranges in which we made the phase-transition concentrations and the diffusion coefficients

vary during such procedure were selected on the basis of the literature on SLES[3]. The red, green, and blue lines in *Figure 13* are the H-L_1, V_1-H, and L_α-V_1 phase-transition front displacements arising from the simulation for which the parameters are such that the sum of the squared differences between the experimental and the numerical data is minimized. A satisfactory agreement holds between the experimental and the numerical data, thus providing a measure of the phase-transition concentrations and of the diffusion coefficients in our system and validating its description through a simple model based on Fickian diffusion. The values of the 3 phase-transition concentrations (in terms of surfactant mass fraction) and of the diffusion coefficients in the 4 phases yielding the curves reported in *Figure 13* are displayed on the top right. Of course, since we made the parameter values vary discretely, the precision of our estimate of the fitting parameters is affected by the incremental steps of the variations we imposed. It is worth mentioning that the order of magnitude of the diffusion coefficients estimated here is consistent with that of the effective diffusion coefficients estimated by Poulos et at.[1] through a different approach. In *Figure 15* in the SI, analogous optical measurements as in *Figure 13* are reported for two samples with different initial surfactant concentration, i.e., 50%wt and 60%wt, and compared with numerical fitting.

Dynamic rheological experiments

In this section, we report the results of the analysis of the dissolution process, using the rheological experimental setup described above.

Transient experiments were carried out with a 70%w/w surfactant paste. Here, we will consider only one specific example, performed isothermally in a plate-plate geometry with plate radius R_i = 4 mm and the gap between

the plates of height h = 0.1 mm. In order to monitor the torque evolution after the addition of (initially pure) water in a controlled geometry, we made a time-sweep test in the linear regime. The experimental results are shown in *Figure 12* along with data from numerical simulations, that will be presented afterward. The torque is reported as a function of time: at very low times, the water addition creates a transient oscillation, which is related to the time needed by the sample rim to reach equilibrium. After the first minimum, the evolution of the torque can be considered as a measure of the dissolution process, by means of the diffusive water in the surfactant paste. The torque passes through a well-defined maximum and then decreases towards significantly lower values. The rise can be explained by comparing *Figure 13* with *Figure 11*, where increasing time results in a decrement in concentration. The maximum can be, then, explained with a morphological transition from the lamellar phase (70%wt surfactant paste) to a cubic/hexagonal phase, whereas the abrupt decrease of the torque depicts the transition to the micellar phase, which is characterized by very low viscoelastic moduli, as already discussed in the previous section.

In order to simulate the dynamic rheological experiment described above, we considered a plate-plate rheometer of plate radius R_i = 4 mm with the gap between the plates (of height h = 0.1 mm) initially filled with a 70%wt surfactant paste. The rheometer plates were surrounded by a concentric pool of (initially pure) water with radius R_e = 24 mm and height h_w slightly greater than h undergoing Small Amplitude Oscillatory Shear (SAOS) flow. Hence its upper plate was subjected to rotation back and forth with velocity

$$v_\theta(r,t) = \gamma_0(r)\omega\cos(\omega t)\, h \quad (10)$$

where □$_0$(r) is the radially-dependent oscillation amplitude, □ = 1/2□ s^{-1} is the oscillation frequency, and t is the time.□□□$_0$(r), in turn, reads

$$\gamma_0(r) = \gamma_{0,\max}\frac{r}{R_\mathrm{i}} \quad (11)$$

with $\gamma_{0,\max}$ = 0.001 the (small) maximum oscillation amplitude (i.e., the oscillation amplitude at the plate border).

If the surfactant paste is modeled as a linear viscoelastic liquid, the shear felt by the liquid under SAOS flow can be expressed as[24]

$$\sigma(r,t) = \gamma_{0,\max}\frac{r}{R_i}\left[G'(c(r,t))\sin(\omega t) + G''(c(r,t))\cos(\omega t)\right] \quad (12)$$

where G' and G'' are the elastic and viscous moduli, respectively. Notice that, as shown by the experimental data in *Figure 11b*, both G' and G'' depend on surfactant concentration, which, in turn, depends on space and time, since, while the rheometer undergoes its oscillatory motion, the surfactant diffuses as discussed above. (We assume that, as the SAOS flow is slow, it provides no additional (convective) mechanism to surfactant dissolution in the flow cell, thus the latter can be entirely ascribed to Fickian diffusion. Therefore, the torque felt by the rheometer rotating plate is

$$M(t) = \int_0^{R_\mathrm{i}} \sigma(r,t)2\pi r dr = 2\pi\frac{\gamma_{0,\max}}{R_\mathrm{i}}\left[\sin(\omega t)\int_0^{R_\mathrm{i}} G'\big(c(r,t)\big)r^3 dr + \cos(\omega t)\int_0^{R_\mathrm{i}} G''\big(c(r,t)\big)r^3 dr\right] \quad (13)$$

In order to calculate M(t), we interpolated the G'(c)- and G''(c)-experimental data in *Figure 10b* through piecewise cubic Hermite polynomials, then we combined such information with the c(r,t)-field arising from the solution of Eqs. 6-9 with the parameters obtained by fitting the optical measurements of the front displacements, as detailed above. We made use of this information to compute the right-hand side in Eq. 13.

In *Figure 14*, the experimental and numerical values of the maximum of the torque absolute value max |M| are reported as function of time, showing

that, as the surfactant paste dissolution goes on during the SAOS flow, the torque at the upper plate first increases, it reaches a maximum, then it decreases until becoming barely measurable. In terms of both the t- and max |M|-scales, a good agreement holds between the numerical and experimental points.

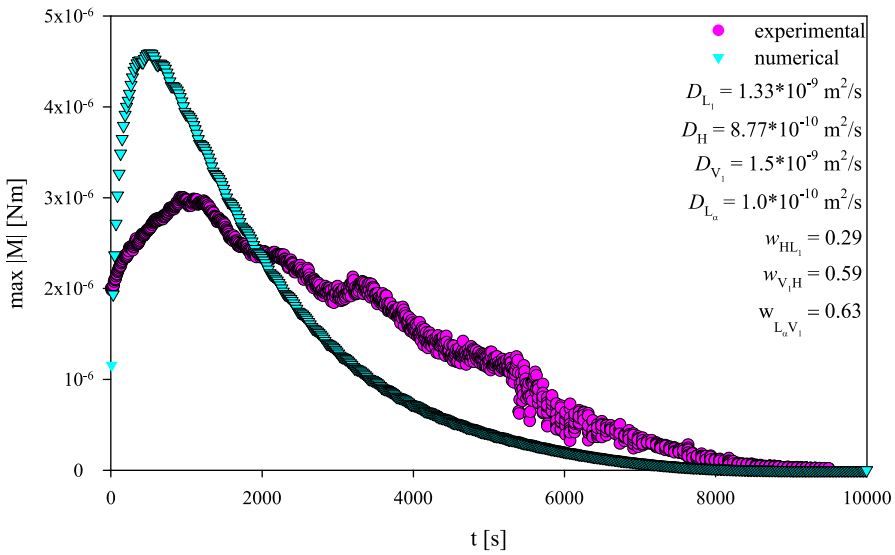

Figure 14 **Maximum of the torque modulus |M| measured by the parallel plate rheometer during the dissolution of a 4-mm-radius surfactant disk. Pink circles: experimental measurements, cyan triangles: numerical simulations**

1.5 Conclusions

In this paper, we propose a multi-technique approach to investigate the dissolution of Sodium Lauryl Ether Sulfate (SLES) in water both in static and flow conditions.

We performed a rheological characterization of the system under steady and oscillatory shear flow that showed non-monotonic changes of several orders

of magnitude in its viscosity and viscoelastic moduli as a function of surfactant concentration.

Time-lapse-microscopy observations on a disk-shaped SLES sample in quiescent water showed water penetrating radially, thus making the sample assume an onion-like radially layered structure where each layer was characterized by a microstructure typical of a different mesophase.

We developed a simple diffusion-based multi-parameter model, by means of which we were able to describe satisfactorily static and dynamic SLES dissolution data at the same time.

The results obtained using the different experimental and numerical approaches are all in great agreement, showing for the first time a comprehensive analysis of the dissolution phenomena of complex surfactant pastes under static and flow conditions. The approach here proposed can provide useful support to the design and optimization of several industrial processes.

1.6 Supplementary

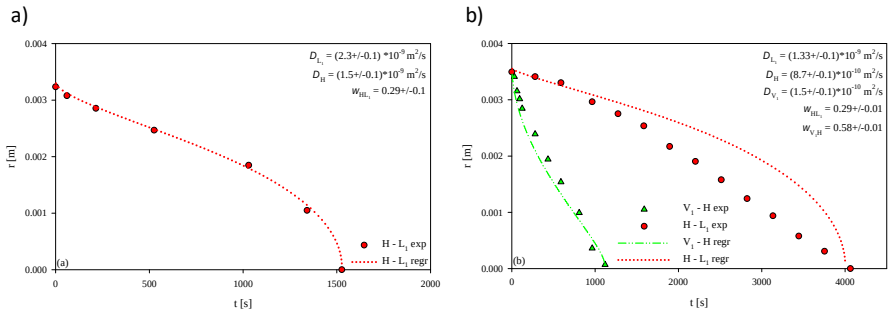

Figure 15 **Radial displacements of the phase-transition fronts during the dissolution of a 4-mm-radius surfactant disk paste with an initial concentration equal to 50%wt (a) and 60%wt (b). Symbols: experimental measurements, curves: Least Squares fits by a Fickian diffusion model (the estimated parameters are reported in each panel on the right).**

In *Figure 15*, analogous optical measurements as in *Figure 13* are reported for two samples with different initial surfactant concentration, i.e., 50%wt (panel a) and 60%wt (panel b). In ***Figure 15****a*, the paste was initially in the

hexagonal phase, thus, while dissolving, it only underwent the L_α-V_1 transition, so only one front displacement appears. In *Figure 15b*, the paste was initially in the cubic phase, so two front displacements appear, as the system underwent the V_1-H and L_α-V_1 transitions, but not the H-L_1, For both cases, we applied the same procedure detailed in the main text to estimate the values of the phase-transition concentrations and of the diffusion coefficients yielding the experimentally measured front displacements and the results are reported on the top right of the two panels in *Figure 15*. From *Figure 15a*, it is apparent that, when only one phase transition is present, there is an almost perfect agreement between the numerical solution and the experimental data, which is still satisfactory for the sample initially in the cubic phase (see *Figure 15b*). From the comparison of the regression outcomes in *Figure 15a-b* and *Figure 13*, it can be noticed that the estimated values of some of the parameters slightly vary from one case to another, yet always being of the same order of magnitude. This can be motivated by the physiological fluctuations of the operating conditions among the different experimental observations.

CHAPTER 2

Experimental investigation of Surfactant Dissolution by direct visualization time-lapse microscopy. Anomalous diffusion mechanisms during surfactant dissolution.

R. Ilaria Castaldo, Chong Gu, Vincenzo Guida, Sergio Caserta, Stefano Guido.

2.1 Introduction

The main surfactants used in several categories of detergent products, including fabric care, home care and beauty care, experience complex phase, and rheology behavior. In standard industrial processing, raw materials are diluted with solvents, such as water, to obtain the final product.

Normally, a thick surfactant paste is broken into small droplets, dispersed into the bulk fluid, and finally dissolved[25]. Critical parameters, such as raw material chemistry, phase equilibria, type of solvent, temperature, and flow conditions play a key role in dissolution processes. Even if the general picture is well accepted, the mechanisms actually governing the breakage step are not well understood. During typical industrial processing, the mixing flow can induce changes of fluid morphology on the micron scale. A key role in these mechanism is played by the interfacial tension among the mixing phases[34]. When viscous stress overcomes droplet cohesive stress, due to the interfacial tension, deformed droplets can break in two, or more, satellites[35]. Alternative mechanisms can be related to surface exfoliation, or tip streaming[36]. Interaction among two or more droplets can, on the other hand, lead to the aggregates formation, or droplet coalescence[37], that can be induced by gentle flow.[38]

Other mechanisms are also active on a molecular scale, both under flow, but also in static conditions. Molecules are transported from one part of a system to another, as a result of random molecular motion[39]. In the presence of concentration gradients, this leads to a net diffusive mass flows, that can be described by typical Fick's law. In the case of diffusion of macromolecules, such as polymers, the variability of diffusive flow with phase concentration can play a role[40]. Concentration variations due to the interaction between dissolving phase and solvent may lead to changes in

molecular morphology, that can lead to complex phase diagram, such as in the case of Sodium Laureth 3Sulfate (SLES)[3]. SLES is a common anionic surfactant found in several categories of detergent products, especially because of its cheapness and its effective foaming agent. During the dissolution process in water, SLES paste undergoes several phase changes[1].

In this work, we want to investigate the dissolution process under flow, in order to better understand which is the control mechanism that drives the phenomenon. To this end, we considered as standard a solution of SLES in water at 70%wt. We designed an experimental setup to visualize the dissolution of surfactant paste in static condition.

In order to investigate the interaction between surfactant and water, experiments on single paste droplets in static conditions were performed.

2.2 Materials and methods

Materials

Alkyl Ethoxysulphate, Sodium Laureth 3 Sulfate (SLES), density = 1.05g/cm^3 and molecular weight = 288.38 g/mol[31], was provided by Procter and Gamble (Beijing, China) 70% in water. SLES was used without further purification. From the phase diagram of SLES [3] in water, four different phases can be observed: a Lamellar phase (Lα) from the raw paste 70% down to 63 wt.%; a cubic phase (V) from 63% to 56%; hexagonal phase (H) from 56% to 31.5%, micellar phase (L) from 28% to CMC (0.0236 %)[41]. In the range 31.5-28% there is the coexistence of L-H phases.

Experimental setup

Dissolution in water of SLES has been examined by Time Lapse microscopy using polarized light. The sample was loaded in a home-made rectangular glass chamber (12.5x8.5x2 cm) placed on the microscope stage. In order to visualize the internal structure and to obtain a fairly well-defined geometry, tiny amount of surfactant paste (2 mg) were squeezed between the bottom glass of the chamber and a coverslip, obtaining a disk-shaped sample with an initial radius of about 2.5 mm. Sample thickness was set to 100 μm by inserting a double-side adhesive tape as a spacer between the two glass surfaces. A fixed amount of water (15 ml) was added in the surrounding chamber in order to observe sample dissolution. Experiments were run at room temperature (about 25°C). In *Figure 16* a sketch of the experimental setup is reported.

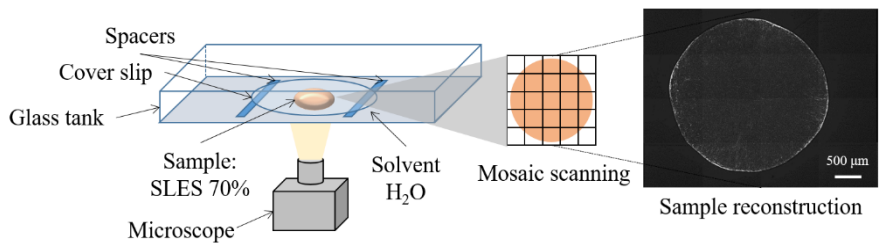

Figure 16 **The cartoon on the left shows the experimental setup: the sample is optically scanned by mosaic imaging (center), the composite image is reconstructed in post-processing (right).**

Time lapse microscopy

The sample was imaged by mosaic scanning, and a composite image was obtained by post-processing stitching algorithms (Image-Pro Plus), a typical example of sample reconstruction is reported in *Figure 16*. Experiments

were conducted by using a Time Lapse video microscopy workstation, based on an inverted microscope (Zeiss Axiovert 200, 5x/10x objective), equipped with a high sensitivity CCD camera (Hamamatsu Orca AG), a motorized stage and focus, controlled by a home-made software, for automatic mosaic scanning of large samples[42]. A Time Lapse routine reiterate automatically image acquisition at a given time interval (1.5 minutes), to allow the analysis of dynamic evolution of sample morphology over time.

Sample description

Amphiphilic molecules, such as surfactants, in solution, can have different spatial arrangements, depending on temperature and concentration, in analogy with what is observed in *liquid crystals*. In nematic phases, molecules are ordered along a specific direction. Smectic (lamellar) phases present ordered planes of aligned molecules. Specific alignment is absent in isotropic phases. When a smectic phase is observed between crossed polarizers, light beams are deviated by the sample structure that can be visualized, unless molecules are aligned orthogonally respect to the optical axis. In this case, black areas ore observed, as it happens in the case of an isotropic medium. The difference between an isotropic medium and a smectic phase can be distinguished observing the sample in conoscopy, i.e. using a Bertrand lens, or more simply by removing the eyepiece and looking down the tube toward the top of the objective. In the case of anisotropic phases, a dark cross (isogyre) is created by the interference of the light beams, due to the symmetry of the refractive index ellipsoid.[43]

Observing raw material (70%) under polarized light, we can see a peculiar texture due to the presence of a lamellar phase, no significant evolution of

sample morphology is observed in the absence of water, a part for a slow evaporation at the border, that can be observed after several hours. Images are reported in *Figure 17a-b* at two different magnifications, maltese cross, due to multilamellar vesicles are clearly visible. Sample thickness was set to 100 µm by inserting spacers between the glass slide and the coverslip, if the sample thickness is increased, it is not possible to visualize the microstructure, due to sample turbidity. In the absence of spacers, the fluid tends to relax in the layer between the glass slide and the coverslip, under its own weight, progressively reducing its thickness. In these conditions, micelles tend to align, forming a web-like texture with wide black areas (*Figure 17c*). Observing the black areas using conoscopy and high magnification objectives (40x), typical isogyre is visible (*Figure 17d*), suggesting phase orientation, due to sample confinement. No structure was visible in conoscopy in the case of 100 µm think samples (*Figure 17d*, insert).

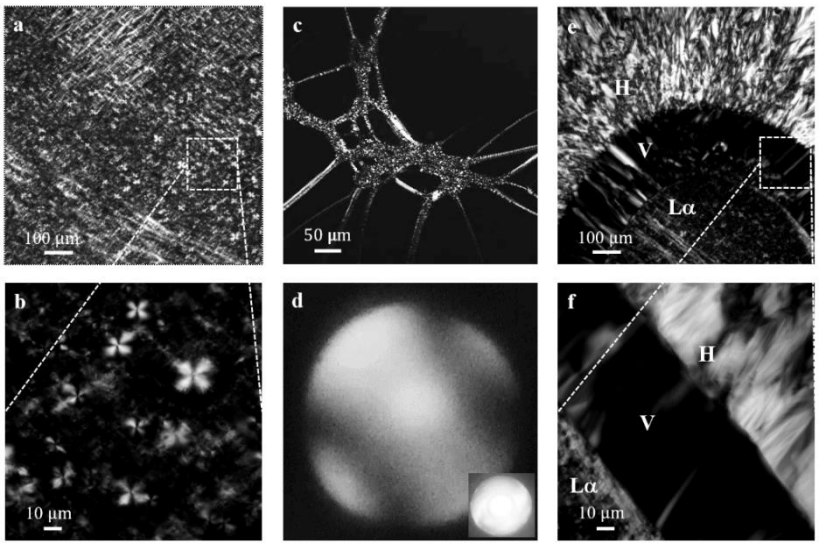

Figure 17 **SLES morphology. Images were acquired using Zeiss Pascal confocal microscope at different magnification (10x a and e, 20x c, 63x oil b and f). Conoscopic images (d) were acquired using a Canon EOS60D camera, removing the eyepieces, and observing the sample down the microscope tube.**

2.3 Results

Adding water in the chamber, the solvent penetrates radially the surfactant paste, that is confined between the two glass surfaces (see *Figure 16*), in the meantime SLES starts to dissolve. Water penetration changes sample concentration and its microstructure. In agreement with the SLES phase diagram, 3 different phases are visible, and the sample during the dissolution process shows an onion-like radially layered structure. An Lα core is surrounded by two V and H concentric shells, while the external phase is a micellar solution (L). In *Figure 16* e and f typical images at different magnification are presented. The circular boundaries between the phases are clearly visible under polarized light. It is worth mentioning that in order to change optics, images e and f were acquired in two different, times from the same sample, due to the dynamic evolution of sample morphology some differences can be noticed.

In *Figure 18* the time evolution of a typical sample dissolution is reported, comparing mosaic images reconstructed from sample scanning acquired at different times. In our experiments, we focused mainly on the initial stage of the process, and only in some cases, the process was monitored up to the complete dissolution of the surfactant disk. The quantitative analysis reported in the following is limited to the first 1 hr.

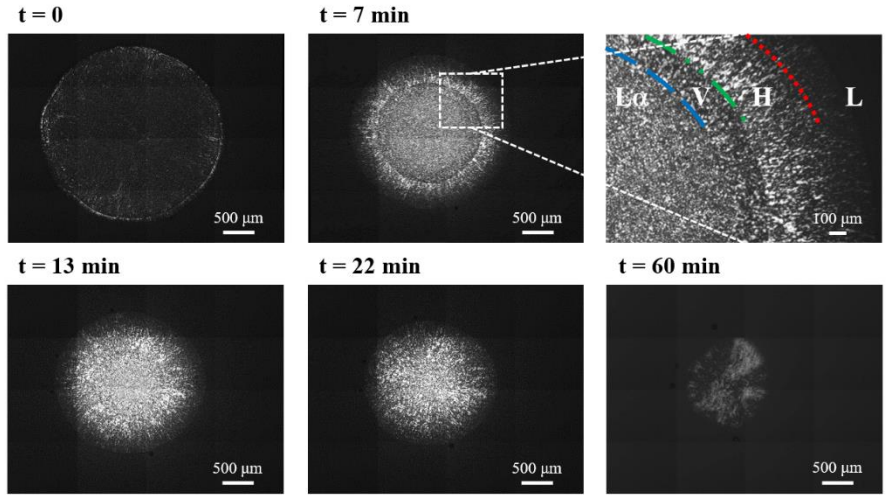

Figure 18 **Typical time evolution of a SLES disk during static dissolution experiments. The image at t=0 was acquired from the raw sample, before water addiction. Other images were acquired at different times. All images were acquired using Zeiss Axiovert 200 microscope, 5x, by mosaic scanning.**

At time 0 a raw surfactant disc presents a uniform morphology, being entirely made of Lα phase. At time 0^+ water was added, and sample imaged at regular intervals. By image analysis techniques, it is possible to measure the evolution over time of interfaces position, that is clearly visible. Interfaces positions are reported as a coloured overlay in the top right image, zoomed from the acquisition 7 min after water addiction. Dashed blue line separates lamellar core from the external cubic layer (Lα-V), dashed-double dotted green line identifies the boundary between the cubic layer and the hexagonal external shell (V-H), finally, dotted red line identify the external boundary between hexagonal and micellar solution (H-L). As reported above, phase diagrams suggest a range of coexistence of H and L phases. In our measurements, we considered the H-L boundary as the limit of the birefringent region, that we can consider corresponding to the boundary of the pure L domain (c.a. 28%wt). As time goes on, the three circular boundaries shrink toward the center of the sample, at the end of the experiment the surfactant paste finally dissolves, leaving only a micellar

solution. During dissolution processes, the (meso)phases observed are typically considered as the equilibrium phases expected at the local composition. This is due to the fact that the transition time between mesophases is typically in the order of 1 second or less, while the evolution of the phases we observe is in the order of minutes, and the entire dissolution process is in our case in the order of about 1 hr. For this reason, surfactant dissolution tends to be considered as diffusion limited processes[9].

Images acquired during the dissolution process were analyzed. For each time step, the position of the interfaces over the entire sample was manually identified, without assuming any imposed shape. The underlying area was measured, and the radius corresponding to an equivalent circle was calculated. In *Figure 19* the radial position of the 3 interfaces, measured from the center of the surfactant sample disk, is reported as a function of time. Experiments were repeated in triplicate, each data point on the chart reports the average of 3 independent measurements, standard deviations are reported as error bars, calculated to take care of fluctuations in the acquisition time (horizontal bars) and variations in the radius estimates (vertical bars). It is worth mentioning some differences are also present in the initial radius of the sample (first red point, at t=0), due to minor fluctuations in the amount of SLES loaded. As time goes on, the radial position of the interfaces decreases. In terms of velocity, it is possible to see that the two internal interfaces (Lα-V and V-H) are faster than the external one. This means the entire process is controlled by the external transition between H and L. By comparing images in *Figure 18* and data in *Figure 19* it is possible to observe that in our experimental conditions, after about 40 minutes lamellar and cubic phases disappear, and the sample is completely constituted of hexagonal phase. In this time frame, the sample radius is

reduced from c.a. 2,5 to c.a. 1,5 mm, a comparable time is further required for the complete dissolution of the sample, and rearrangement of the hexagonal phase in micellar solution.

We made control dissolution experiments starting from pre-diluted pastes at 60 and 40% wt SLES in water. The 60% sample was initially in the cubic phase, and presented only two phase transitions, while in the 40% case the initial phase was already hexagonal, and no internal phases boundary was observed, data not shown for the sake of brevity.

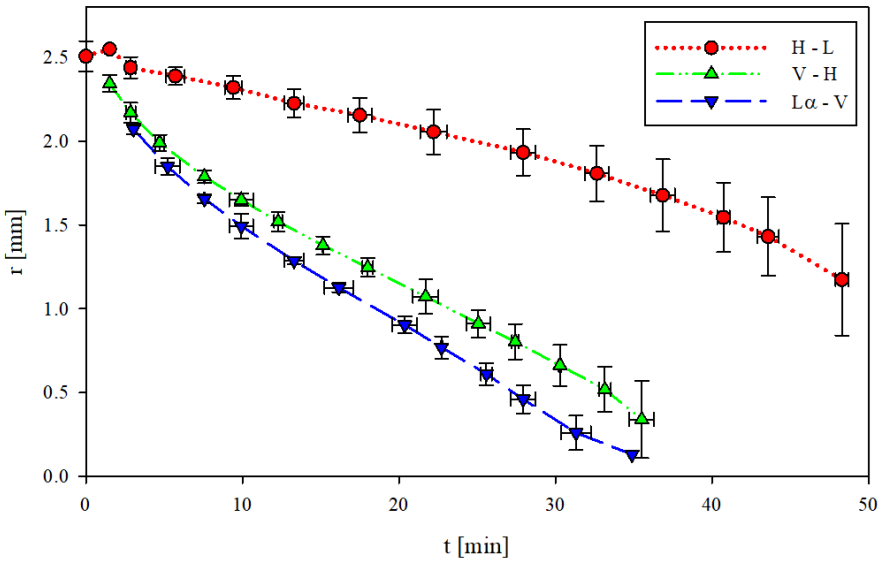

Figure 19 **Position of interfaces between different phases during dissolution. Red circles, green up triangles and blue down triangles represent the boundaries between hexagonal and micellar (H-L), cubic and hexagonal (V-H) and lamellar and cubic (Lα-V) phases, respectively. All interfaces decrease their radial position as a function of time, the outer (H-L) is the slower.**

By careful visualization of sample images during the dissolution process, a dynamic rearrangement in the sample texture over time can be observed (see Video 1 and Video 2). In particular, a radial movement of the surfactant phase can be noticed. To quantify this phenomenon, we added 2 drops of

Polystyrene microbeads suspension in water (Polybead® 4.5 μm diameter, SD 0.15 μm, 2.7% solid) to 10ml of surfactant paste, the sample was mixed manually and degassed by centrifugation (Heittich Rotanta 460, 3000rpm for 15 minutes) to remove air. In order to verify the influence of particles size and material, experiments were repeated using monodisperse (Cospheric, SiO2 MS – 1.8 g/cc, 7.75 μm monodisperse, 3.7%CV) and polydisperse (Cospheric, Isospheres 0.60 g/cc, 5-30 μm TiO2 coated) silica particles. In this case, 0.02g of dry particles were added to 5ml of surfactant paste, mixed and degassed with the same procedure. No significant differences were observed.

Sample internal motion was tracked by measuring particle position on every frame as a function of time, by image analysis. In *Figure 20*, the evolution as a function of time of the radial position of the 3 phase transition interfaces measured in one of the experiments is reported (blue dashed, green double-dotted, and red dotted lines for the Lα-V, V-H, and H-L interfaces, respectively). In the same chart, the radial position of microbeads from the same experiment is also plotted as a function of time (black lines). At time 0, particles are in different radial position, being random distributed over the entire sample. As time goes on, during the dissolution process, particles move along the radial direction, as a consequence of the bulk motion of the suspending surfactant paste. In particular, as the Lα-V interface approaches, beads slightly move toward the center of the sample, i.e. the radial position decreases. Once Lα-V and V-H interfaces cross the position of the beads, an acceleration in the positive radial direction is observed, the motion is gradually slowed down, particles stay fixed in most of the Hexagonal phase, and finally the motion is reversed, being directed toward the extern of the sample (radial position increases as a function of time), as the H-L interface

approach particles. After crossing the H-L interface, i.e. once they arrive at the micellar phase, particles are free to move, due to the reduced viscosity of the surrounding fluid. The amplitude of movements of the particles suspended in the paste is limited to a few microns, and is poorly visible over the entire scale of r axis in *Figure 20*, for this reason in the top right inset, a zoom is reported, to better appreciate the measurements. A qualitative description of the phenomenon also is reported in the cartoon on the right, in *Figure 20*. The colored circles represent the 3 interfaces, shrinking during the dissolution, different speeds of the interfaces are referred to by the different length of the colored radial arrows. Black dots represent microbeads, randomly distributed over the sample. Black arrows describe the trajectories of the beads, that initially move toward the center, and then revert toward the boundary. It's worth mentioning the particles motion observed is qualitatively consistent all over the sample, but the displacements appear wider in the case of particles initially located close to the external boundary of the sample, i.e. at high values of r, while particles initially close to the sample center (low values of r) are approached by the Lα-V interface at later times, and exhibit only a limited shift from their initial position. A role in this difference could be related to the radial curvature, that can be neglected in the case of external particles, while could be more relevant for the inner ones.

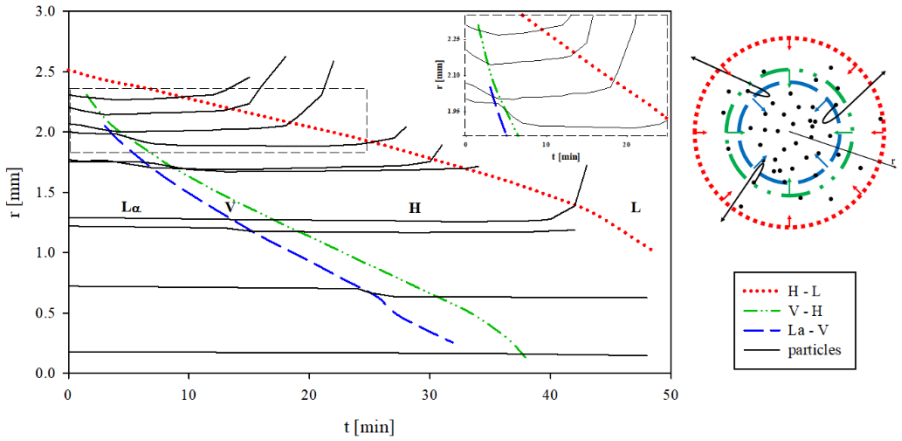

Figure 20 **Anomalous motions of beads inside the sample during dissolution. Zoom of initial instant time and cartoon with complexively description.**

To better investigate the radial movement of the surfactant paste during the dissolution process the mass flows of water and surfactant were estimated from interfacial positions measurements reported in *Figure 21*. We assumed the mass concentration in each of the concentric regions to be an average value of the phase range suggested by the phase diagram[3]. For example, since the lamellar core of the sample is expected to span in a concentration range between the initial 70% and the transition concentration of 63%, we assumed a uniform concentration of 66.5% over the internal core of the sample. Analogously we estimated the concentration in the intermediate cubic annulus to be 59.5%, and the concentration of the external hexagonal rim to be 43.5%. Given these values and the measured position of the interfaces, we calculated the variation of SLES and water mass within each of the interfaces, as a function of time. In our calculation, we neglected the limited difference in density between water and SLES. This estimate of the mass accumulation corresponds to a measure of the (IN-OUT) flow, according to standard mass balance. The graph in *Figure 21* is relative to the three interfaces (H-L, V-H, and Lα-V, from top to bottom). In each chart

SLES and water mass flow are reported as a function of time (open and closed squares, respectively), the overall flow is also reported (colored symbols, in agreement with previous charts). It is worth mentioning the overall mass flow calculated as the sum of water and SLES flow along each of the interfaces, is also in agreement with the volumetric flow, calculated as simple volume reduction, without any assumption on the phases concentrations.

We can notice that all the flows are systematically negative, i.e. both the SLES and the water diffuse from the centre of the sample toward the external solvent domain as the surfactant disk dissolves. Only in the initial minutes, the water flow along the H-L interfaces is positive, i.e. the water is diffusing from the external solvent toward the hexagonal rim. This water flow might result in a pressure shock along the negative radial direction that could contribute to the movement we observed in the particles.

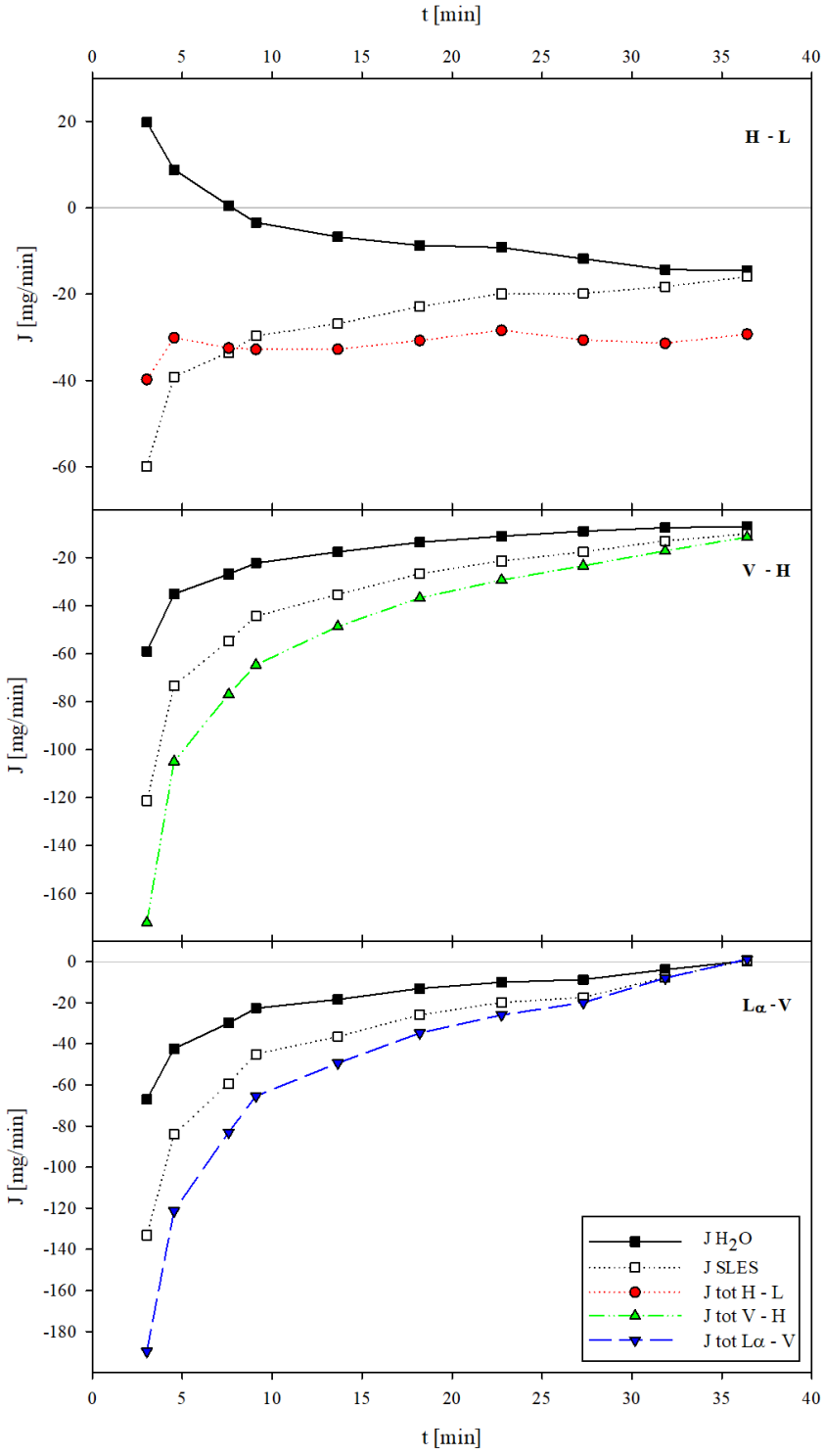

Figure 21 **Water and SLES flow among different phase transitions.**

Particles motility suggests the presence of stress profiles along the radial direction, in the different phase domains, related to the mass flow. To investigate this aspect, the size and shape of deformable air bubbles, residual after sample degassing, was measured by image analysis techniques[44]. In *Figure 22* typical images of a bubble are reported. As the dissolution process goes on, the interfaces move toward sample center, crossing the bubbles (*Figure 22a*), that show different morphologies in the different phase domains. Bubbles initially present in the lamellar phase (*Figure 22b*) appear spherical, as expected in the case of isotropic pressure. As bubbles cross the Lα-V interface, they appear deformed, assuming an ellipsoidal shape with a mayor axis orthogonal to the r direction, and parallel to the interfaces, suggesting the presence of a non-uniform stress profile that is compressing the sample along the radial direction in the cubic region. In *Figure 22c* a typical image is reported, where the bubble boundary is overlaid in white, and the mayor and minor axes are identified as *a* and *b*, respectively. In the later steps of the process, the hexagonal phase reaches the bubbles, that change abruptly their shape, remaining still ellipsoidal, but with the mayor axis oriented along the radial direction. This shape suggests a stretching of the sample along the radial direction, that can be explained considering that the V-H and H-L interfaces are moving at different velocities, in particular, the inner interface is faster than the outer, as a consequence the hexagonal ring experiences an extensional flow along the radial direction. In *Figure 22e* it is possible to observe the bubble crossing the H-L interfaces, two different lobes of the bubble are visible, that appear to have different size and shape, as consequence of different stress profiles in the two domains. In the micellar phase, bubbles recover finally their spherical shape but show a size higher respect to their initial one (*Figure 22f*).

A quantitative analysis of the bubble deformation and orientation can be done by measuring the geometrical parameter that defines the size and shape of the observed ellipsoidal morphology. For each frame images are segmented, bubbles area identified, and the mayor and minor axis (*a* and *b*, *Figure 22c*) of an equivalent ellipse calculated by image analysis techniques. Bubbles deformation can be quantified by calculating the deformation parameter ($D = \frac{a-b}{a+b}$), in agreement with typicthe al analysis of small deformation of isolated droplets in liquid-liquid mixtures[45]. The angle α of the mayor axis a, respect to the tangent to the closest interface was also measured (*Figure 22d*). α is 0 for bubbles elongated orthogonally to the sample radial direction, and is 90° for ellipsoidal bubbles oriented along the radial direction. By assuming the third axis of the droplet (not visible in our setup) to be equal to the minor axis (b), i.e. assuming bubble shape to be a rotational ellipsoid, an equivalent radius was calculated by volume conservation ($R = \sqrt[3]{\frac{ab^2}{8}}$) for each time step.

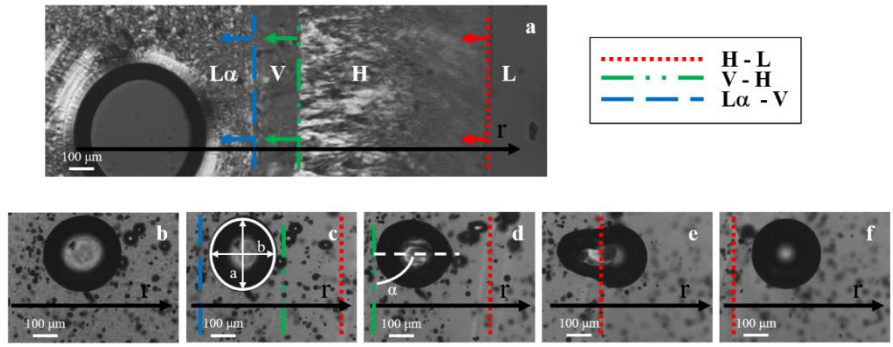

Figure 22 **Bubbles' deformation through different phases. In order to visualize the presence of the interfaces, image (a) was acquired with cross polarizers. is shown in sequence, these images were acquired in the bright field.**

In *Figure 23* the typical evolution of the bubble shape parameters is reported as a function of time during the dissolution process. In the data here reported

the initial surfactant disk radius was about 6mm, as a consequence, the dissolution process required a longer time. The deformation parameter D is plotted in the top chart, α in the central diagram, while in the bottom chart a and b are reported as normalized respect to the initial value of the droplet diameter ($2R_0$ = 93 μm), the equivalent radius, normalized respect to the initial size is also reported (R/R_0). Blue coarse, green medium, and red fine patterned areas are superimposed to the charts to indicate the finite time range required by the Lα-V, V-H, and H-L interfaces respectively to completely cross the bubble. During the transition between the two phases bubble rearranged their shape. In the initial step, bubbles in the lamellar domain appear spherical, with a deformation parameter almost 0, and α not defined. As bubbles approach the Lα-V interface, after an initial rearrangement, they increase their size, still remaining spherical ($a \cong b \cong 2R$, $D \cong 10\text{^-}3$). As soon as Lα-V interface touches the bubble, a compression along the radial direction is observed, bubble assume an ellipsoidal shape with the mayor axis parallel to the interfaces ($\alpha \cong 0°$). After the transient, once entirely in the cubic phase, bubble only partially relax their deformation ($D \cong 0.01$), continuing to increase its size. In the following step of the process, the bubble is reached by the V-H interface. The bubble is stretched along the radial direction ($\alpha \cong 0°$), and the deformation is progressively increased, until bubble touches H-L interface, when it relaxes back to a spherical shape, suggesting the final recovery of isotropic stresses in the micellar phase. In the hexagonal phase, bubble size is almost doubled respect to the initial value ($R/R_0 \cong 2$), and remains almost constant in the remaining steps of the process.

The pressure in the droplet can be estimated from its volume, assuming isothermal ideal gas behavior ($P/P_0=V_0/V$, *Figure 23*). The pressure of the

bubble in the lamellar phase is about 5 times the value measured in the hexagonal and micellar phase. The pressure in the bubble is higher than the pressure in the surrounding sample, due to the interfacial tension between the surfactant paste and air (Laplace). Assuming this value to be weakly dependent on sample concentration, at least in the range 70-56%, data suggest that the internal core of the sample is compressed by the surrounding layers.

Being the system isothermal, this relevant variation in the pressure can be directly related to differences in the Gibbs free energy (dG=VdP-SdT), and hence to the chemical potential.

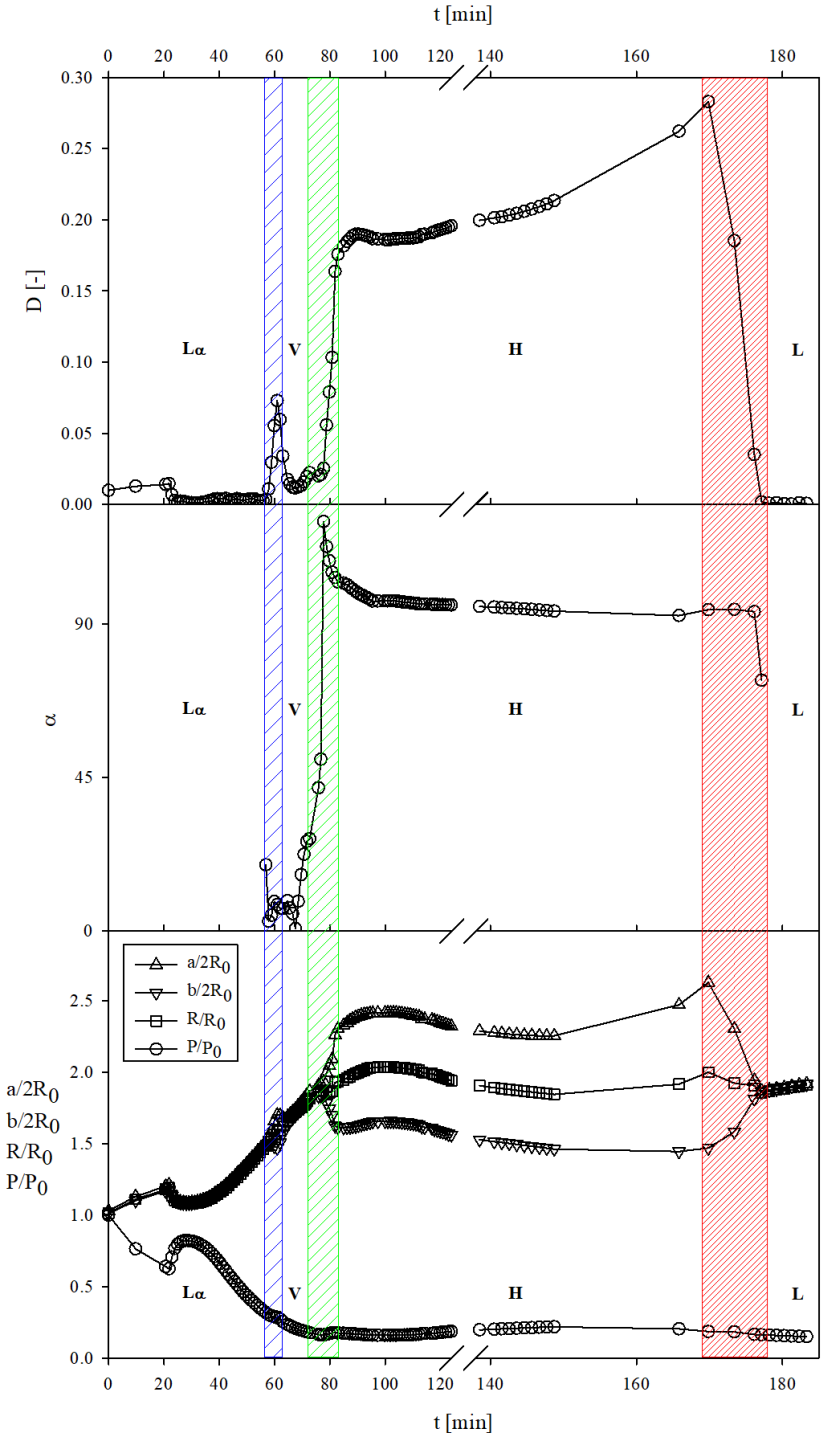

Figure 23 **Bubble size and deformation parameters during the dissolution process.**

2.4 Conclusions

In this chapter, an in-depth study of the static dissolution of the SLES has been carried out. From the tests carried out the forward speed of the fronts was measured, from this measure it is clear that the transition from the hexagonal to the micellar phase is the slow step that dominates the time evolution of the entire process.

Furthermore, the size and shape of air bubbles present in the sample was investigated. As soon as the surfactant comes into contact with water, the sample seems to be under a compressive stess, as evident by the analysis of the bubbles deformation. This phenomenon is also supported by the observation of movement of particles used as a tracer. During the dissolution process, the phase equilibrium fronts move toward the center of the surfactant disk, when the bubbles are hit by the cubic phase, they undergo a compression, while passing through the hexagonal phase they undergo an elongation.

A possible explanation of the observed process can be attributed to the Marangoni effect. The Marangoni effect is associated with two surface phenomena, the motion in a fluid interface due to the local variation of interfacial tension caused by differences in composition or temperature induced for example by a dissolution (or evaporation) of a solute, and then the departure from equilibrium tension, produced by dilatational deformation of an interface[46].

CHAPTER 3

Dissolution of complex surfactant paste under controlled microfluidic flow.

R. Ilaria Castaldo, Chong Gu, Vincenzo Guida, Sergio Caserta, Stefano Guido.

3.1 Introduction

Sodium Lauryl Ether 3 Sulfate (SLES) is a detergent of great industrial interest. It is an anionic surfactant, widely used in many people's care products (soaps, shampoos, toothpaste, and products for baby care). It is appreciated for being an excellent foaming agent and cheap. Industrially SLES is typically available in water solution, at high surfactant concentration (70 % w/v). SLES 70 appears as a viscous paste with a slightly yellow color, and it is soluble even in hard water. But during its dissolution with water, pastes with lower SLES concentration show gel structures which are typical of ether sulfates.

Industrial processing of surfactant-based materials typically includes a water dissolution step. It is well established that both physicochemical and rheological parameters, such as raw material chemistry, type of solvent, temperature, and flow conditions, play a key role in the dissolution process. After the addition of water, the viscosity first increases rather rapidly, when the surfactant concentration is reduced to a level below 30 % it decreases considerably (see *Figure 11* Chapter 1). Water-SLES solution remains pasty down to 28%, while lower surfactant concentrations result in a liquid-like fluid with a very low viscosity. Normally SLES concentration in finished commercial products is lower than 26%, but the final viscosity can be adjusted and increased to the desired value, accordingly to the needs. According to the final composition, electrolytes, polymers, co-surfactants, hydrotropes, co-solvents, oil, perfume, and others can be added.

Surfactant aggregation, chemistry, type of solvent can affect the detergent behavior, both during surfactant making and during dissolution from the raw material paste to the finished products.

The dissolution step is usually run under flows of various intensity, coupling high shear mixing sections and stirred tanks, to induce breakage of paste in tiny fragments, and to facilitate transport efficiency on the solvent side.

The mechanisms active during this process are not well understood. In particular, it is not clear what are the control resistances to mass transport during the dissolution process under flow.

For this reason, a microfluidic setup has been developed to investigate the dissolution process of SLES pastes under controlled flow conditions.

3.2 Materials and methods

Materials

Sodium Laureth 3 Sulfate (SLES), an anionic surfactant prepared by ethoxylation of dodecyl alcohol, then converted to a half ester of sulphuric acid and neutralized by conversion to the sodium salt[11] was provided by Procter and Gamble (Beijing, China) 70% in water and used without further purification. Phase diagram of SLES [3] in water shows formation of four different phases, starting from lamellar phase (L□) at high concentration (from the raw paste 70% down to 63 wt.%) to micellar phase (L), concentration range widely used in finished product (from 28% to CMC) passing through cubic(V) and hexagonal (H) phase (respectively from 63% to 56% and from 56% to 31.5%).

The sulfate end group (SO_4) is representative of the hydrophilic head. The number n indicates the average quantity of oxyethylene units present in the compound; generally, in commercial products, its value is in between 2 and 3. SLES is prepared by the ethoxylation of dodecanol (or lauryl alcohol,

$C_{12}H_{25}OH$). The ethoxylate is converted to sulfate ester and finally salified with sodium ions.

Cellulose fibers were used as thickeners to obtain a viscous water solvent for the dissolution experiments. Cellulose fiber slurry was provided by P&G, the composition was unknown, but the solid concentration was estimated to be 1.5% w/w by water evaporation. The slurry appears as a concentrated odorless whitish high viscous slurry. Fibers added to a miscible liquid, they tend to make the mixture optically thicker and more viscous, inducing a relevant change in the fluid rheology. The cellulose fiber slurry was used as untreated, and labeled as Ci = 100%, and diluted with bidistilled water, obtaining samples with concentrations 1, 5, 15, 30 % w/v of the raw slurry. Corresponding to a solid residue of 0.015, 0.075, 0.225 and 0.45 grams in solution respectively. The solutions were prepared by mixing the raw slurry with water in a beaker using a magnetic stirrer. It's worth mentioning cellulose fibers are not stable in water, as they tend to separate by sedimentation in a time that depends on the fiber concentration, i.e. on the fluid viscosity being, for our samples, always higher than hours. For this reason, in all the experiments here reported fluids can be considered to be stable for the entire duration of the experiments.

Experimental setup

Dissolution tests have been carried out in a homemade microfluidic device, consisting of a plexiglass cell made of two plates, with a glass visualization window. The lower plate has a 0.8 mm cavity in which a 35x60 mm coverslip glass (150 μm thick) is placed, the top plate, on the other hand, is shaped with a central window of 23x23 mm that is closed by a 1 mm thick glass, the two plates are connected by screws, sailing is guaranteed by a 1

mm thick rectangular rubber frame that is pressed between the two plexiglass plates. Internal thickness δ of the resulting rectangular flow chamber is guaranteed to be 200μm by a spacer and verified by microscopy. Fluid inlet and outlet to the flow chamber are provided by two connectors placed before and after the visualization window. During each test, 2.0 mg of sample were preliminarily inserted in the central point of the cell, sample weight was controlled by a 4-digit precision scale. Once the two plates were sealed a disk-shaped surfactant paste sample, of controlled thickness (200 μm) and radius (typically 2.4 mm ± 0.2 mm, that means in term of area approximatively 18 mm^2) resulted in the center of the visualization window.

Approximating flow cell geometry to a rectangular channel with a width of 60 mm and height of 200 μm, and assuming the solvent as a Newtonian fluid, for each imposed flow rates, the values of the shear rate can be estimated as:

$$\dot{\gamma} = \frac{\dot{Q}}{A * \delta}$$

Eq. 1

where $\dot{Q}$ is the imposed flow rate, A is the cross section of the rectangular channel and δ is the channel thickness.

In the dissolution tests under flow, in order to guarantee a constant flow rate of the solvent entering the flow cell, a syringe pump, Harvard Apparatus PHD Ultra was used. Two plastic syringes with a diameter of 29 mm and a maximum volume of 60 mm were used. The solvent is inserted into the syringes, which are connected to the cell by a rubber connector system; once the flow rate has been set, the fluid enters the free volume of the cell by investing the surfactant disc and exits through the outlet hole, the latter in turn connected to a collection beaker.

Using the "Withdrawn only" command, the solutions, used as a solvent, were loaded into the syringes; these solutions were then sent to the dissolution system using the "Infuse only" command, once the flow rate has been set.

Tests were conducted using different flow rates in the range 1 - 50 ml/min, and different solvents. 3 different values of flow rates were imposed: 5, 10 and 20 ml/min, that correspond to nominal values of shear rates of 42, 84, and 168 s^{-1}, respectively.

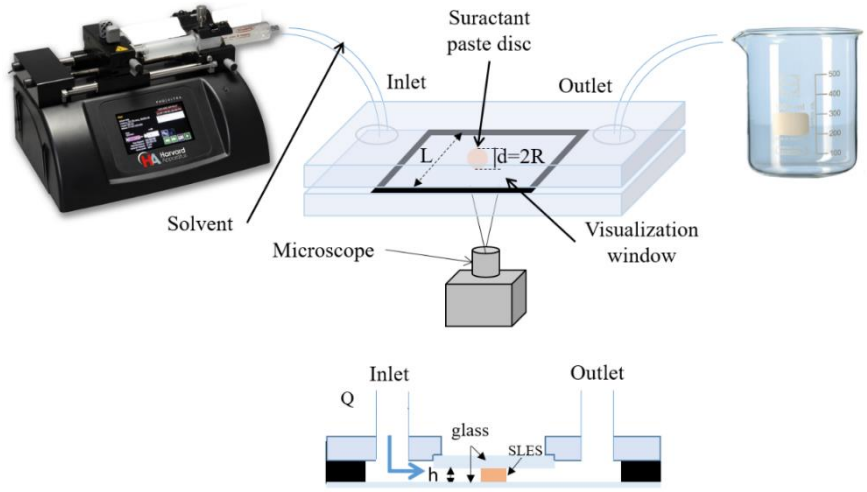

Figure 24 **Experimental setup cartoon, home-made microfluidic device (side view on the bottom), with syringe pump to push the solvent inside and beaker at the end to collect the out coming flow.**

In a first experimental campaign, simple bidistilled water was used as a solvent. In a second-time water solutions were used, to obtain fluids with different chemical-physical properties. The first type of solutions consisted in premixed water-SLES mixtures, (in the range 5, 10 and 20 %wt). The second type of solution consisted of a water dilution of a cellulose fibers slurry.

The details of the complete experimental campaign are reported in **Table 1**.

Time lapse microscopy

The evolution over time of the dissolution process was followed by using a Time-Lapse optical microscopy system that allows continuous observation of phenomena occurring on very long time scales, from hours to days. For this purpose, it was used an inverted optical microscope (Zeiss Axiovert 200) with 5x objective (Zeiss CP Achromat PH1).

The microscope has a motorized stage controlled by a homemade software. Images are acquired through a monochrome CCD camera (Hamamatsu Orca AG) and sent to a personal computer through a firewire interface. The digital image consists of a 1344x1024 pixel matrix. The value of each pixel, between 0 and 255, is equal to the brightness of the corresponding point in the image. The entire workstation is governed by a control (Objective Imaging) that can be controlled by a computer using a Time-Lapse software operating in the Labview environment. This software allows periodic scanning of the entire sample or specific areas of it. It is possible to acquire bidimensional images or a z-stack of images (in case of three-dimensional observation). In this case, it is necessary to fix the thickness of this matrix and the number of planes (layers) in which you want to divide the thickness; in these tests, there were no scans along z. As input data, it is necessary to manually select the field of view of the sample of interest using an electronic joystick and set the time interval between two consecutive scans. In the same field of view, it is possible to acquire more images, thus generating a mosaic. Once started, the program stores the coordinates of the field of view and controls the motorized glove table. At the end of each scan, the program remains paused until the next iteration for a range set by the operator. The scanned images are saved on the hard disk. At the end of the experiment, by reconstructing the mosaics, a series of images is obtained that can be

used to obtain a sequence that describes the evolution of the sample over time.

In all tests, the flow cell was placed on the microscope stage. Once the field of view of the sample is manually identified, various images are acquired through which it was possible to generate a high-resolution mosaic, representative of the entire surfactant disc. The delay time between two successive scans was set depending on the solvent used and the imposed flow rate, in order to obtain an adequately refined sampling of the process. The test started (time = 0) when the solvent was introduced into the cell and stopped when the whole surfactant disc was completely dissolved.

Rheology

Rheological measurements of the solvent solutions consisting of water and different amount of SLES or cellulose fibers of different concentration have been carried out. Cellulose fibers were used to obtain more viscous solutions, without changing the chemistry of the solutions, thus understanding how the presence of the fibers could affect the process.

Rheological measurements of different SLES concentrated solutions have been carried out with Discovery HR-3 hybrid rheometer.

Rheological measurements of cellulose fibers solutions were done using an Anton Paar MCR 702 Twin Drive rheometer with 50 mm diameter cone-plate geometry.

For rheological characterization of SLES, samples at several concentrations were prepared from 0.1% w/v to 25% w/v. For each sample, steady-state tests have been run for 1 minute, at 3 different shear rate (10, 50, 100 s-1); In the concentration range, 0.1-25% the fluid presents as a uniform micellar

phase, that can be considered as Newtonian. In fact, no time effects were observed in the measurements, and the average value of the viscosity measured for each imposed shear rate was the same, the value measured at 100 s-1 is reported in Figure 25.

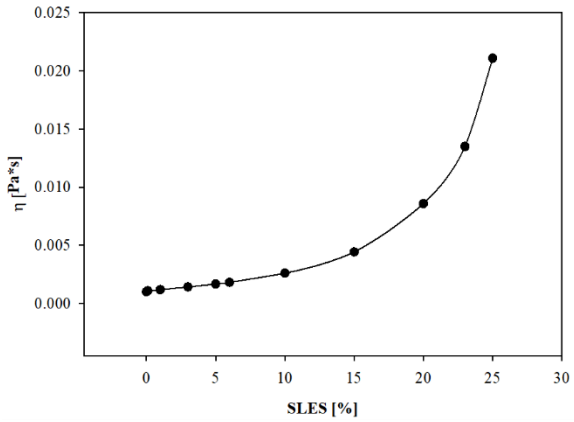

Figure 25 **Viscosity of SLES solution at different concentrations.**

For cellulose fiber solutions, flow curves have been run varying the shear rate in a range of 0.01 to 100 s^{-1}. Each value was measured out of an integration time was of 10 seconds. Flow curves for 1% cellulose fiber solutions were traced back, i.e. from the highest to the lowest shear rate, and without pre-shear. For all the other solutions, however, the curves have been outlined taking into account the pre-shear, data are reported in *Figure 26*.

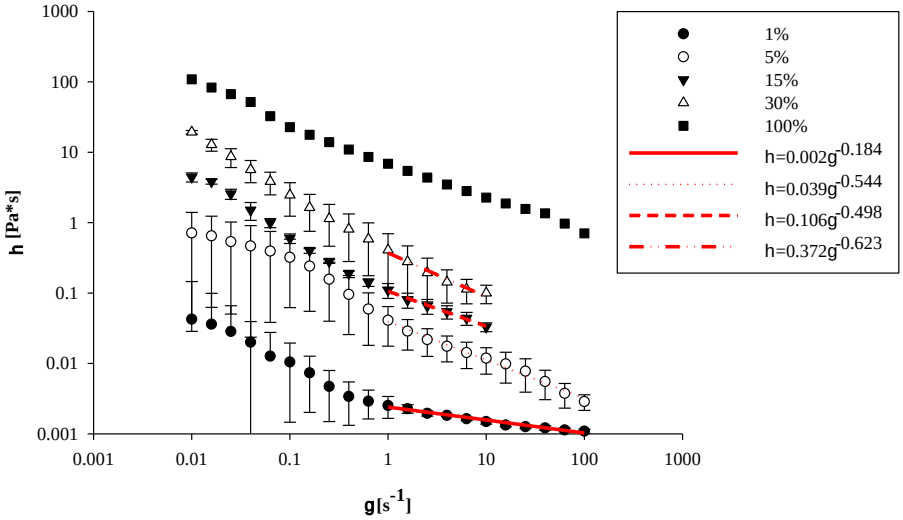

Figure 26 **Rheology of cellulose fibers solution at different concentration.**

As can be seen from *Figure 26* the cellulose fibers solutions in water, have a strong shear thinning behavior. The viscosity of the systems varies from a minimum of 0.001 Pa*s up to a maximum of 100 Pa*s, as a function of concentration and shear rate. Each sample, at constant fiber concentration, the viscosity span a range of about two decades in the range of shear rates 0.01-100 s-1. For shear rate higher than 100 s^{-1}, the system has considerable instability; in fact, a collapse of the curves down to water viscosity is observed, due both to the non-Newtonian behavior and to fibers settling on the bottom of the plate during the tests, for this reason, no data at very high shear rates have been reported. On the other hand, very low shear rates (<1s-1) are not relevant for our experimental setup, being far from the values effectively imposed during the industrial dissolution process. For this reason, we focused on the range 1-100 s-1, where rheological measurements can be effectively described by a power law behavior. The fit of rheological data is reported in the *Figure 26*.

In order to try to estimate the viscosity of the systems for different cellulose fibers concentration, and per each flow rate, a trend line from experimental data has been extrapolate for shear rate of interest.

At this point, fixed the fibers concentration, the viscosity values that approximately the solvent solutions should have at varying shear rate, can be calculated from these equation:

- $\eta = 0.002*\gamma^{-0.184}$ for a fiber concentration of 1%;
- $\eta = 0.039*\gamma^{-0.544}$ for a fiber concentration of 5%;
- $\eta = 0.106*\gamma^{-0.498}$ for a fiber concentration of 15%;
- $\eta = 0.372*\gamma^{-0.623}$ for a fiber concentration of 30%.

The table below shows the details of the tests carried out. In particular, for each type of solution used (water, water with the addition of a given concentration of SLES, or water with a given percentage of cellulose fibers) the values of the shear stress at the wall are reported per each flow rate tested, calculated as the product of the shear rate at the wall and the viscosity of the medium for the same value of the shear rate. Tha table is sparse, it means that not all the flow conditions have been tested for all the solutions. This is because in some conditions, such as when using cellulose fibers, the flow can be so strong to drag and detach the surfactant disk from the slide. For this reason it is not always possible to follow the dissolution under flow; on the other hand, concerning the solutions with different concentration of SLES, tests have been carried out only for a single intermediate value of flow rates (5 ml/min). Future work could be devoted to investigate also at different flow rates.

Shear stress [Pa]		FLOW CONDITIONS						
		1	5	10	20	50	100	$\dot{Q}$ [ml/min]
		8.4	42	84	168	421	842	$\dot{\gamma}$ [s^{-1}]
TYPE OF SOLVENT	Pure water	0.008	0.042	0.084	0.168	0.421	0.842	
	1% cf	-	0.051	0.089	0.157	-	-	
	5% cf	-	0.214	0.294	0.403	-	-	
	15% cf	-	0.691	0.979	1.387	-	-	
	30% cf	-	1.521	1.974	2.565	-	-	
	5% SLES	-	0.070	-	-	-	-	
	10% SLES	-	0.109	-	-	-	-	
	20% SLES	-	0.360	-	-	-	-	

Table 1 **shear stress calculated per each solution at different flow conditions.**

Viscosity increases with the fiber content but reduces with the shear rate. For the systems considered all the solutions and estimated shear rates, the viscosity varies from a minimum of 0.001 Pa*s (pure water) to a maximum of 0.015 Pa*s, the highest values found for a shear rate of 42 s^{-1} considering 30% of cellulose fibers. In the speed range considered, the viscosity of a system containing within it 1% of cellulose fibers can be considered almost constant and close to the viscosity of the water.

For each solution (considering fiber or SLES concentration), and each shear rate, shear stress can be defined as $\tau = \dot{\gamma} * \eta$

Like viscosity, stress also increases as the fiber concentration increases, but it shows a difference that is different from the shear rate. Increasing the speed, in fact, there is also an increase in shear stress, which is obvious since the stress is directly proportional to the speed. The most marked variations with the speed are found for systems with a higher slurry content.

Firstly, it's necessary to make a brief consideration about the fluids used as solvents in the dissolution tests, in particular from a rheological point of view.

Undoubtedly water is the simplest one, both from a chemical point of view (its interaction with the surfactant paste in static condition has been deeply described in previous chapters), and from the rheological point of view (it is a Newtonian fluid with very low viscosity).

Adding a certain amount of SLES in water, the fluid is still Newtonian but viscosity slightly increases up to 10% SLES w/v (about 1 order magnitude), higher concentration result in a strongher increment in viscosity, up to a value 100 times higher than water when the concentration is 20% w/v. For all these concentrations the system is in the micellar phase.

Regarding cellulose fibers solutions, the scenario is different and things are more complicated. Firstly, fibers represent a non-homogeneous system; in water, they tend to settle in a range of time that varies according to their concentration. Settling time has been tested to be less than the time necessary to run the test (regardless of concentrations and flow rate conditions examined). Therefore, for their inhomogeneity and their size, fibers' behavior does not reflect a Newtonian fluid, on the contrary, they are strongly shear thinning. Despite the strong thinning behavior, it is possible to note a trend in the viscosity as a function of the fibers concentration. Fixing shear rate at 10 s^{-1} the viscosity increases as the concentration increases, see *Figure 27*.

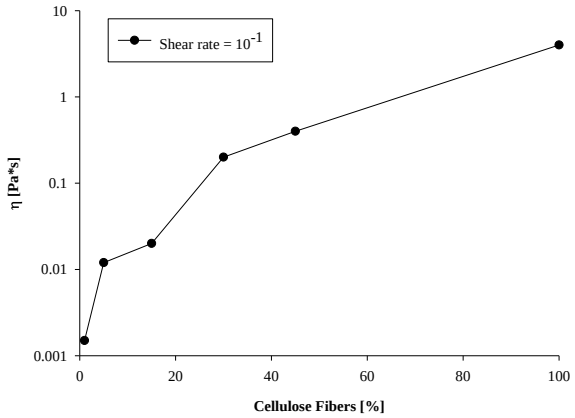

Figure 27 **Viscosity of cellulose fibers solution, at fixed shear rate.**

Data analysis

In order to proceed with the reconstruction of the mosaics and, subsequently, to analyse the experimental data, a commercial software Image-Pro Plus was used.

Digital images acquired during Time-Lapse experiments have been dragged into the image area and processed through the commands in the toolbar. Images necessary for the reconstruction have been loaded as input data and then overlapped together, the procedure was repeated for all sets.

Merging all the reconstructed images, they were used to generate a sequence describing the dissolution over time of the surfactant paste disc. Subsequently, experimental data have been obtained by image analysis of the disk paste area over time from the first dry set to the end; manually the sample contour has been highlighted and then with the measure tool it is possible to choose the measures to be carried out: area, major axis, minor axis, maximum diameter, minimum diameter, average diameter, center of mass X, center of mass Y. Not all these measured parameters were used for

this type of analysis, so far just the evolution of the area was automatically reported in an Excel file, for subsequent analysis. The procedure was repeated for all the images constituting the considered sequence.

3.3 Results

Flow test results

In *Figure 28*, as an example, some images are reported for some conditions tested at different times. It is possible to observe how the effect of flow is strong even at a lowest flow rate, indeed characteristic dissolution time is strongly lower than the one in static conditions. When flow rate increases, the effect is stronger and SLES dissolves quickly. Observing sample shape under flow, it is possible to notice that when the flow rate is low (e.g. 1 ml/min) the sample keeps tanking the disk shape during dissolution, but when flow rate increases, the sample start to change its shape and it becomes like a bullet oriented in the flow direction.

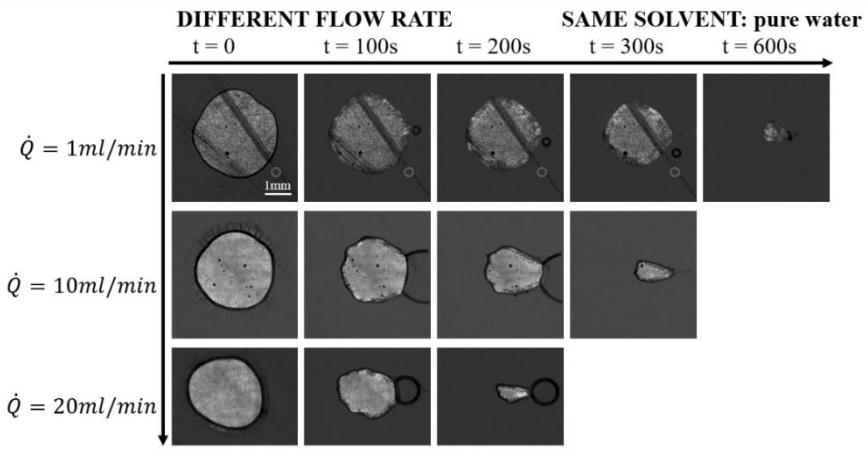

Figure 28 **Example images of dissolution over time of SLES in water at different flow rates.**

Even under flow, interaction with water causes, as well as in static condition, the formation of transition phases; as always SLES is initially in lamellar phase, after adding water three different mesophases start to appear. Observing the sample, detailed images, and additional information will be reported as supplementary materials, as time goes by two interfaces can be identified and their position monitored over time can be calculated their speed and the distance between the two that roughly represents the thickness of the hexagonal phase. It is possible to see that the thickness of the hexagonal phase is different according to the flow direction. In particular, once hexagonal phase layer is formed, the thickness remains constant all over around the sample, despite position at the end of the sample (right side, according to the flow), in this side the hexagonal phase looks like growing over time; a possible explanation of this phenomena is that it is like the internal interphase of that layer tends to go towards the center, according to what happens also in static dissolution, but at the same time, the other side (the external one) it is pulled by the flow, and forced to go in its direction; this does not happen in the other 3 positions where the flow direction and the interfaces movement are in agreement.

Basically, observing what happens at the small scale during dissolution under flow, suggests a hypothesis, namely that the phase transition between hexagonal and micellar is accelerated by the flow because the only difference in thickness of the H-L transition can be seen in the downwind position where the flow is weaker.

In order to compare results between different solution, trends over time of the sample area, normalized respect to its initial value, are reported.

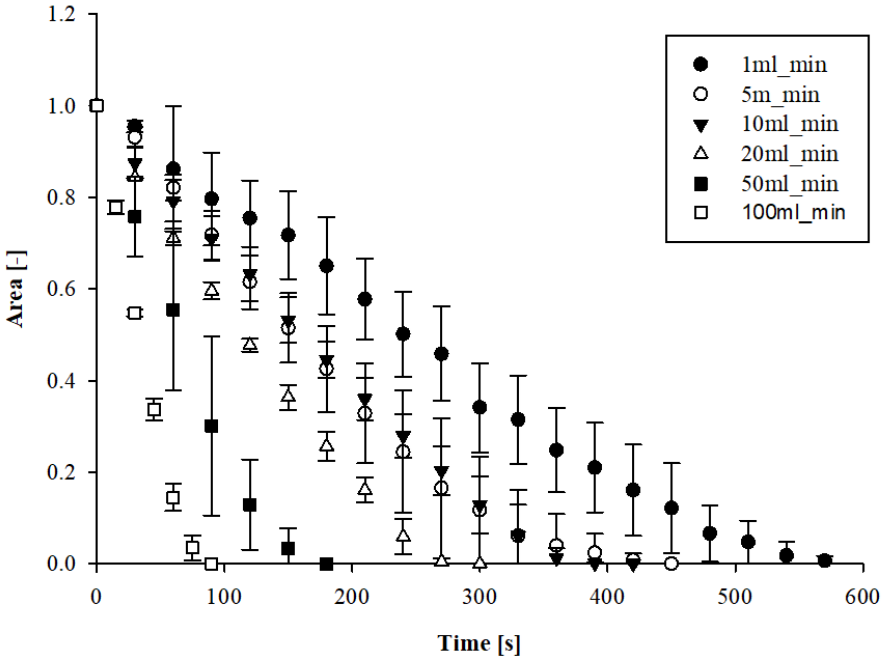

Figure 29 **Evolution over time of SLES in water at different flow rates.**

According to *Figure 29*, the effect of flow rates is evident, the higher is the flow the less is the dissolution time.

Subsequently, considering that in reality, during the dissolution process, the solution, made of water and other substances, doesn't have a constant concentration; in fact, while SLES melts it passes into solution, where the concentration becomes gradually higher and higher, this involves 2 effects, on one hand, the fluid viscosity increases with the concentration, and, on the other hand, the driving force, proportional to the concentration gradient between the 70% surfactant drop and the bulk solution, decreases; these two effects have different impacts on the dissolution process.

In order to see the effect of increasing surfactant concentration in the solution used as solvent, as said before, solutions with different

concentration of SLES (5, 10 and 20%) have been prepared and setting the flow rate at a value of 5 ml/min, a comparison between the different dissolution times was carried out.

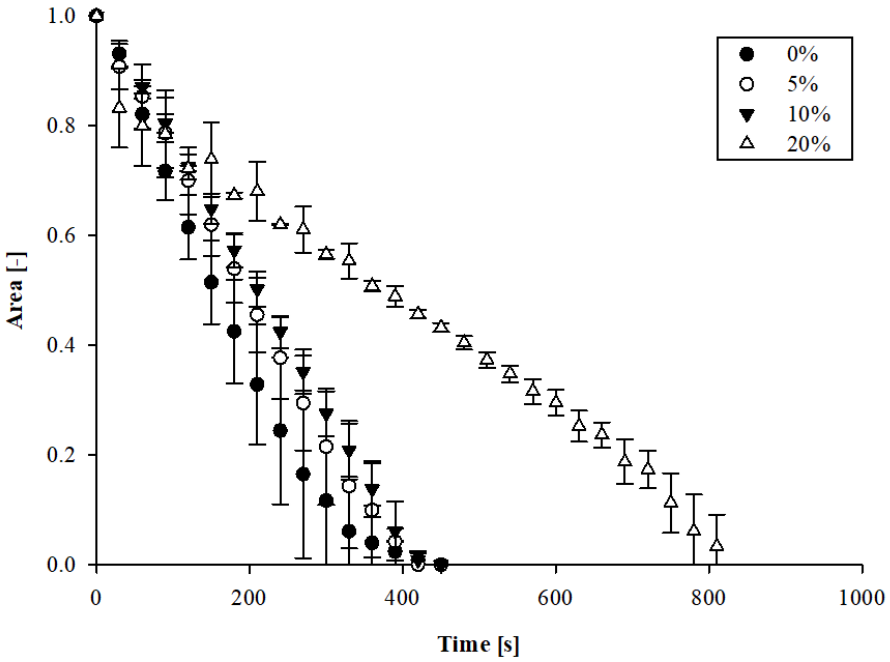

Figure 30 Dissolution time of SLES at the same flow rate in water with different solution.

In this case what can be observed from comparison between different solvents and water, dissolution time doesn't change significantly if SLES concentration in water is 5% w/v or 10% w/v, even if it is a bit higher than water, on the other hand in the case of 20% w/v SLES solution dissolution time increases significantly.

In order to evaluate the effect of a more viscous system without change the chemistry of the solvent, or the concentration gradient, as explained above, different cellulose fibers concentration solutions have been tested. In order to understand the effect of viscosity for different flow rates,

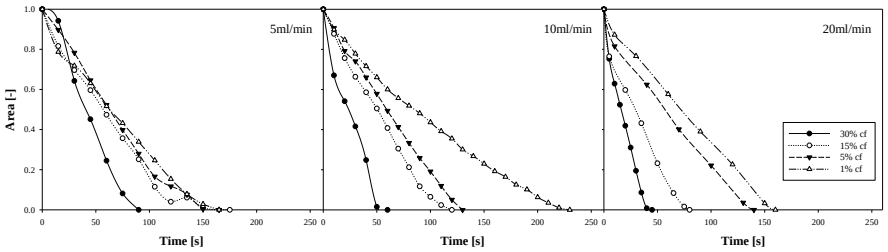

Figure 31 **Panel with effect of fibers concentration on dissolution for each tested flowrate.**

As can be seen from trends shown in *Figure 31*, for any given value of the imposed flow rate, i.e. keeping constant the imposed shear rate, as the concentration of fibers increases, the dissolution time decreases. This means that increasing the slurry percentage, that reflects an increase in the viscosity, an acceleration of the dissolution process is observed.

Results in *Figure 31* shows also a variation of the slope of the curve under some conditions. Indeed, in the case of higher flow rates, a more marked reduction of the sample area is observed in the initial instants of the process; it looks like if initially, the surfactant dissolved more quickly.

It's worth mentioning that it was not possible to use raw fibers slurry (100% sample) as solvent solution, since it was not possible to follow the dissolution process for the entire experiment because after an initial time, once the sample size was reduced due to the dissolution, the undissolved paste was dragged out from the solution flow. This problem was found for all the flow rate considered and was attributed to the strong drag force, due to the relevant viscosity of the flowing solution. For this reason, data were considered unreliable, and not reported. No similar behavior was ever observed in the case of diluted fibers solutions, whose viscosity is several orders of magnitude lower respect to the raw slurry.

The differences observed in the dissolution time obtained imposing different flow rates, or different solvents having different viscosity have a

common trend. We observed a reduction of the dissolution time by increasing the imposed flow rate, i.e. the shear rate on the sample, but also by increasing the solvent viscosity. For this reason, we estimated the shear stress on the surfactant disk sample, as the product the nominal value of the imposed shear rate (Eq. 1) and the viscosity of the solution at the corresponding value of shear rate. In *Figure 32* the dissolution time, calculated as the time the surfactant disc need to disappear, is reported as a function of the imposed shear stress, for different experiments run using different solvents and imposing different flow rates.

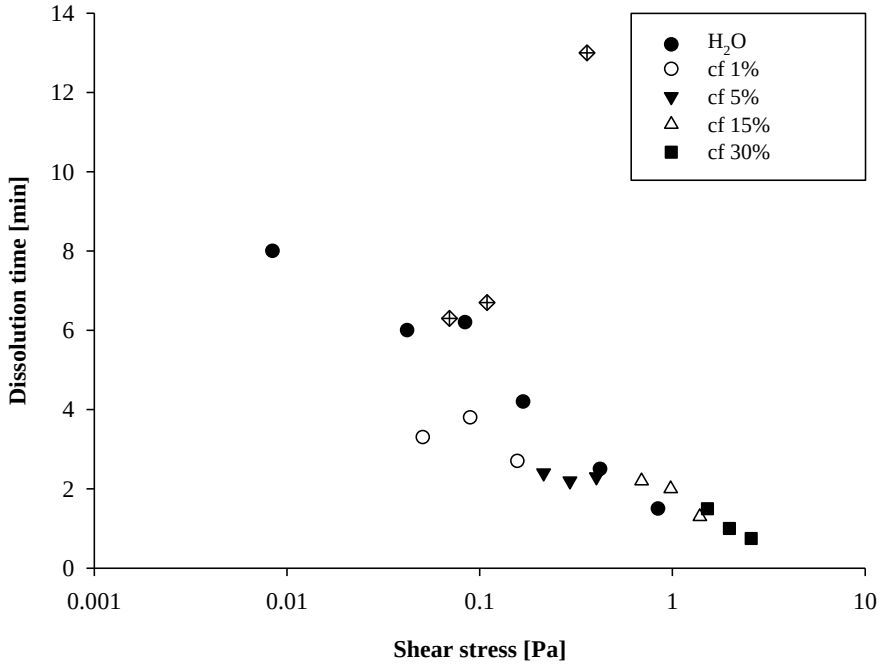

Figure 32 **Dissolution time over shear stress for all the conditions tested.**

An increase in flow rate and viscosity both contribute to accelerating the dissolution process; while increasing the concentration of SLES in solution, even though the viscosity of the solution increases also in this case, as can be seen from the graph in *Figure 32*, the dissolution time does not scale with

the stress in the same way as the other results, this leads us to think that the driving force prevails over the flow rate.

3.4 Conclusions

The objective of this work was to study the dissolution process of SLES applying the effect of flow and comparing results between different solvents. In particular, the effect of flow on dissolution was evaluated from the microscale of a single paste droplet, but the aim is to extrapolate information that is not limited to the simple micro-fluidic cell but could also be applied on an industrial scale optimizing the industrial process.

From the experiments conducted, we tried to. In fact, it has been attempted to draw out a more general pattern of the characteristic parameter of the process, namely the dissolution time.

The experimental procedure involved the use of a Time Lapse video-microscope system to perform image acquisition. This experimental technique has allowed us to continuously follow the dissolution process and to trace a quantitative evolution of the sample's temporal evolution.

Firstly, a first consideration has to be done is that the flow strongly influences the dissolution process; dissolution time of the same surfactant droplet in static conditions is significantly higher. Increasing the shear rate, there is a considerable reduction in the dissolution time.

From the tests carried out it was observed that the use of fibers, which lead to an increase in the viscosity of the system, has a positive effect on dissolution. The characteristic times are reduced compared to the case in which the solvent is simply water and this reduction is even more marked when the percentage of these substances is greater. However, what can significantly make the process slower is an increasing of the bulk fluid

concentration, which reduces the gradient force and leads to higher dissolution time.

3.5 Supplementary

As it possible to see in the *Figure 33*, there is an asymmetry in the sample during the dissolution in the flow direction, the higher is the flow rate the more evident is the bullet like shape oriented in the flow direction. Moreover, the internal morphology does not vary in the same way but depends on the position under examination. To try to quantify the flow effect, 4 different positions have been identified (upwind, downwind and 2 sides) as shown in the figure. Finally, even if the internal phases cannot be clearly determined, two interfaces can be identified: the external one (red) which almost certainly represents the phase transition between hexagonal and micellar, and the internal one (green) that represents the transition between lamellar and hexagonal; it is not easy to verify whether the cubic phase is formed in the flow. By monitoring the position of these interfaces, their speed over time has been calculated and the effect of the flow rate has been checked and finally, the thickness of what is presumably the hexagonal phase has been measured, noting that this is different above all in the downwind zone.

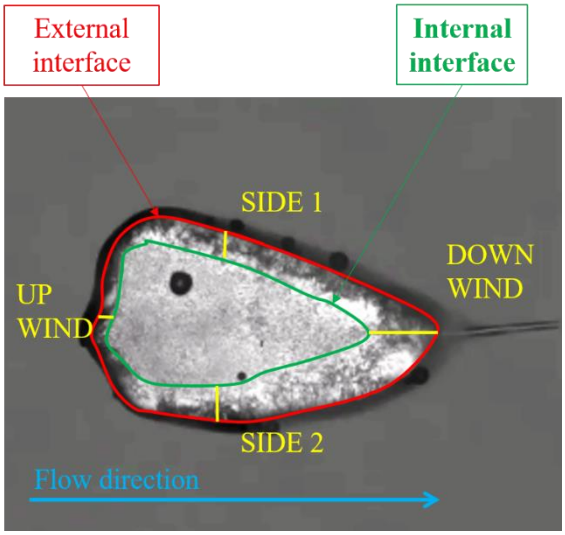

Figure 33 **Surfactant disc paste droplet during dissolution under flow, the edge between phases are highlighted with two lines.**

As time goes by two interfaces can be identified and their position monitored over time; the distance between two interfaces that roughly represents the thickness of the hexagonal phase. The thickness of the hexagonal phase is different according to the flow direction. In particular, once formed, the thickness remains constant both in the upwind position and in the two sides, while in the downwind position it tends to grow, as if on one side it tends to go towards the center, but at the same time it is pulled by the flow, which instead does not happen in the other 3 positions where the flow direction and the interfaces are the same. Monitoring the position of these interfaces, as it has been done for static conditions, their speed can be estimated, but in this case there are substantially no differences between the external and the internal one, differently from what it is possible to observe in the static case, where the external interface speed was significantly smaller than the internal one. Basically what it has been observed is that the phase transition between hexagonal and micellar is accelerated by the flow. Also, in this case, the only difference is seen in the

downwind position where the flow is weaker. This is part of a complex phenomenon, so more research is required.

Another aspect that is interesting is also an effect of the flow; as it possible to observe in down-wind position, and it is even more evident in the *Figure 34* below; during dissolution, under flow, there is a surfactant wake induced by flow. The higher is the flow the thicker and consistent the filament is, and as soon as the flow stops it disappears.

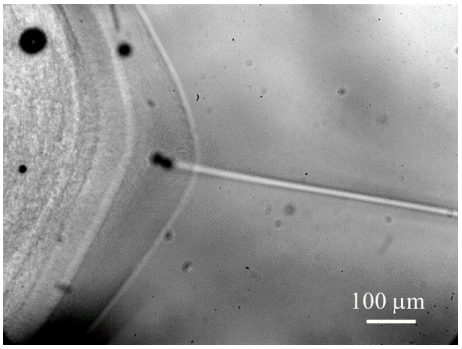

***Figure 34* Detail of surfactant filament forming in the flow direction.**

CHAPTER 4

Scale up of dissolution processes from microfluidics to pilot plant.

R Ilaria Castaldo, Chong Gu , Vincenzo Guida, Sergio Caserta, Stefano Guido.

4.1 Introduction

Industrial processing of surfactant-based materials typically includes a water dissolution step. It is well established that both physicochemical and rheological parameters, such as raw material chemistry, type of solvent, temperature and flow conditions, play a key role in the dissolution process. Breakup in complex fluids where interactions between mesoscopic structural features can affect the flows remains poorly understood and a burgeoning area of research[47]. Considering the great industrial interest, this study was carried out with the aim of the understanding the effect of flow on the dissolution of SLES.

4.2 Materials and methods

Materials

Sodium Laureth 3 Sulfate (SLES), is the same used for static dissolution test and for experiments carried out in microfluidic flow cell, described before in previous chapters

Experimental setup

Lab test setup

Preliminary experiments of dynamic dissolution have been carried out, putting 1 mg of SLES on the bottom of a glass tank, 500 ml of distilled water have been added and a blade agitator is used at different stirring speeds (400–200 and 100 RPM), the blade is completely immersed in water but is not in contact with the sample. A conductivity meter (Eutech Pc 2700) is inserted in the tank to check the process measuring conductivity during dissolution. On two opposite sides of the tank, two sheets polarizers have

been attached crosswise, on the back of the tank a lamp is placed and on the opposite side the images are acquired with a high definition camera. *Figure 35* shows a scheme of the setup used.

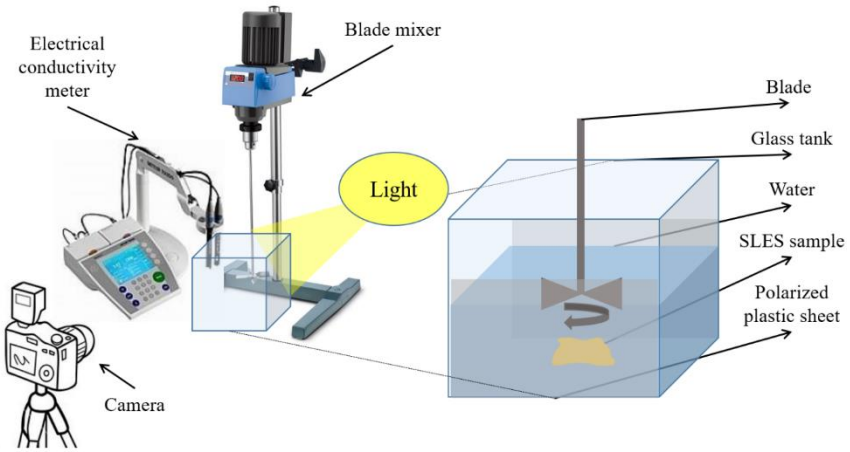

Figure 35 **Medium scale dissolution test of SLES in water, dissolution is measured with a conductivity meter.**

In order to study thoroughly the dissolution kinetics of the surfactant under flow, tests were conducted using 3 different speed: 100, 200, 400 rpm. For these tests, simple bidistilled water was used as a solvent.

Subsequently, the glass tank has been replaced with a beaker, and a wider range of experimental conditions have been tested. In particular, the speed range investigated goes from 30 to 2000 rpm, and different concentration conditions have been tested, e.g. starting from pure water to a final concentration of 15% of SLES w/v, or starting from a solution of SLES in water at different concentration (i.e. 10, 15, and 20% w/v) other 5% of SLES was added.

On top, a more precise and accurate test method was developed, that could somehow be connected to results obtained in the microfluidic setup, described in the previous paragraph, and whose results could somehow be used for the scale-up; instead of conductivity meter, a Raman probe has

been used, just some conditions have been tested, in particular, 3 speeds were selected (100, 500 and 1000 rpm) and 4 different concentration ranges have been tested (from pure water to 5 or 15% of SLES w/v or from 5 to 10 or from 10 to 15).

Pilot plant setup

The aim of this work was to scale up the results obtained in the lab test to the pilot plant scale. For this experiments, the setup summarized in the cartoon in *Figure 36* has been used.

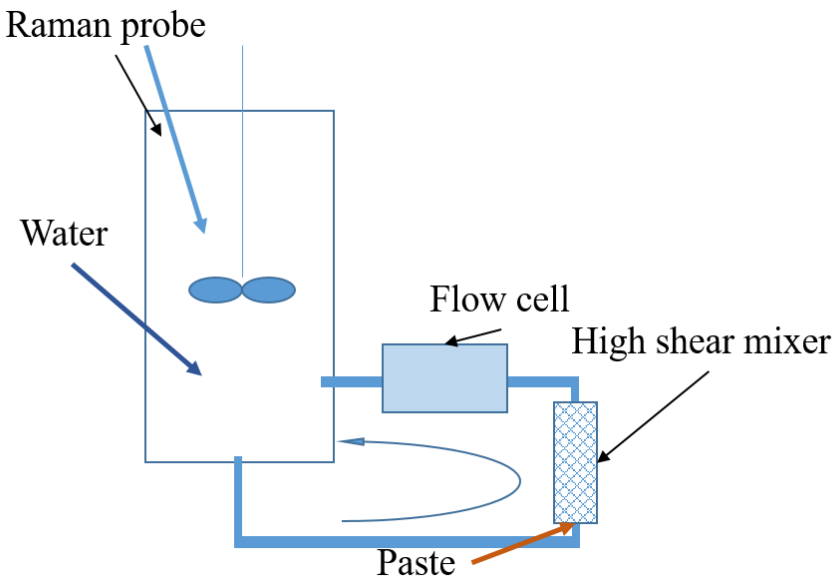

Figure 36 **Pilot plant setup cartoon.**

In a 200L batch, a 20cm of diameter blade is inserted, and speed set at 50rpm the batch is filled with water for different final volume, based on the test. The batch is liked with a rotor pump that pushes raw material (surfactant paste at 70%) into the system at 0.38 kg/min, passing through a high shear mixer whose flow rate was set at 1000rpm. A recirculation system is created with a cable system, the recirculation flow rate was set at 5kg/min. After the high shear mixer and before the batch, a flow cell was

inserted to observe the particle size during dissolution. The system was controlled with a PLC. Inside the batch, the same Raman probe used for the lab test was inserted.

For all the test, the batch was filled with water, enough to reach the final desired concentration, then, paste was injected, with the same flow rate, for a period of time long enough to put the right amount for each test; every test was separated into 2 parts: first parts of the test are necessary to reach different intermediate concentrations (from 2.5% w/v to 22.5%), in a second step the same amount of SLES was added (1.2 kg ± 0.2 kg). All the details are reported in the table above.

H2O	I AES [kg]	time [min]	C_1 [%]	II AES [kg]	time [min]	C_f [%]
24.107	0.893	2.350	2.5	0.963	2.534	5
22.321	2.679	7.049	7.5	1.040	2.737	10
18.750	6.250	16.447	17.5	1.238	3.258	20
16.964	8.036	21.147	22.5	1.368	3.601	25

Table 2 **Summary table with SLES and water concentrations used for each test**

Raman

In the *Figure 37* are presented spectra of SLES at different concentrations in the 300-1800 cm^{-1} spectral region. This region contains the typical peak associated to OH bending mode of water (labeled as δ(OH)) at 1600 cm^{-1}, the bending mode of CH_2/CH_3 groups (labeled as $\delta(CH_2)/\delta(CH_3)$) at 1440 cm^{-1}, C-C stretching mode at 1300 cm^{-1} and 760-910 cm^{-1} range and a big envelope (1000-1150 cm^{-1}) associated to SO_4^{2-} bending mode. The three latest peaks (at 750, 560 and 420 cm^{-1}) are due to MR probe signal that is as much evident when the measured signal is not very high to cover it. Raman spectra were measured with a direct immersion Raman probe (Raman MR-RXN1 Analyzer; Kaiser Optical System Inc.) with a laser

wavelength and power of 785 nm and 350 W, respectively. The spectra were at a resolution of 1 cm^{-1} and an integration time of 15s.

As expected, the intensity of specific peaks increases with SLES concentration.

The CH_2/CH_3 and CC peak at 1560 cm^{-1} and 1300 cm-1, respectively, are not affected by the contribution of the peaks associated at probe spectrum (black line in figure below) and thus used to determine a calibration curve, reported in the top right of *Figure 37*; in order to reduce the noise, both integration areas are divided by integration area of water for each specific concentration.

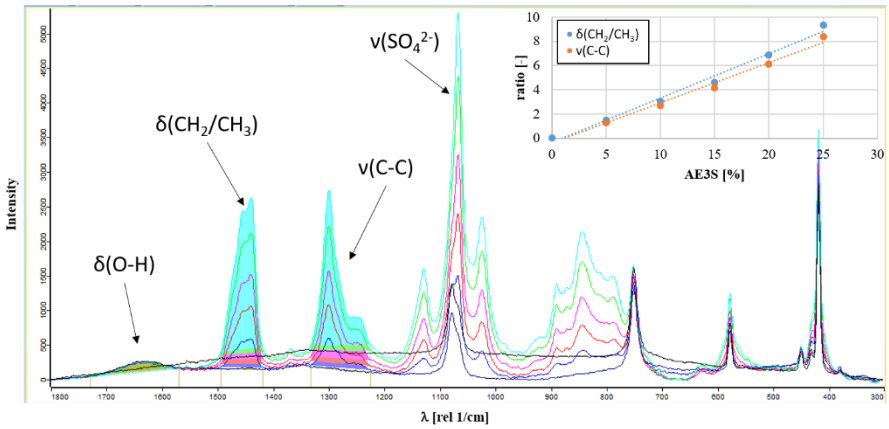

***Figure 37* Raman spectra of SLES in water solution at different concentrations. The calibration curve obtained by spectra analysis is reported in the top right of the figure.**

4.3 Results

Conductibility measure results

By monitoring the conductivity as a function of time, it is possible to follow the dissolution process. From the graph in *Figure 38* it is possible to see that

as the stirring speed increases, the conductivity value reaches a plateau value in less and less time.

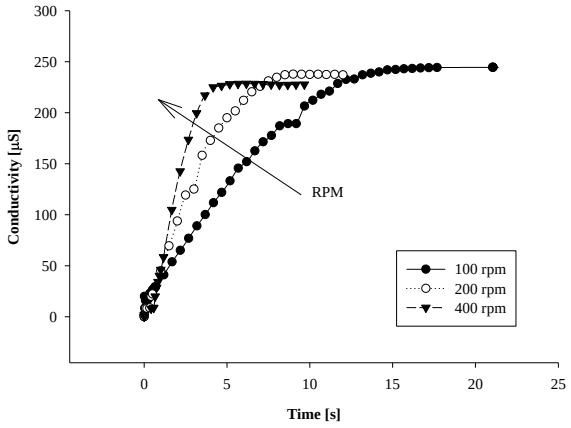

Figure 38 **Conductivity curves during the dissolution of SLES in water at 3 different agitation speed.**

Fitting the conductivity data with dissolution equation reported above, it is possible to estimate a characteristic dissolution time, see *Figure 39*.

$$C(t) = C_0 + C_f[1 - e^{-\alpha t}]$$

Where:

- C(t) is conductivity over time
- C_0 is conductivity at the beginning
- C_f is the final value
- α is equal to $1/t^*$, with t^* is the characteristic dissolution time

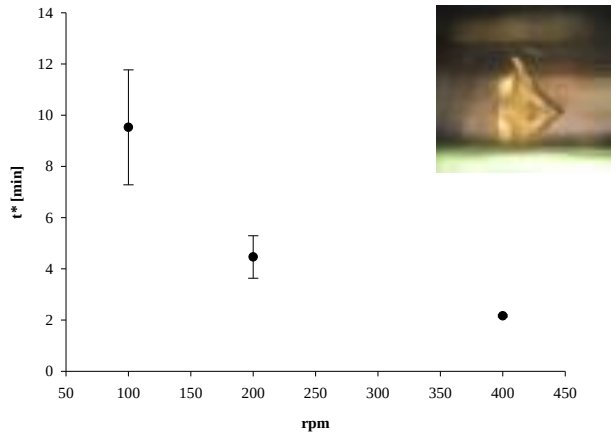

Figure 39 **Characteristic dissolution time at different speed, estimated by conductivity measurements.**

At characteristic dissolution time, which reduces with increasing stirring speed, it is possible to see, as shown in the inset in *Figure 39*, that the remaining amount of SLES which has yet to be dissolved is practically comparable for all the stirring rates tested.

Lab test results

Observing what happens in a beaker, dissolution time was calculated as the time at which the quantity of SLES put in solution had completely disappeared. In *Figure 40* results of all conditions tested are reported. Each curve represents the time necessary to dissolve a certain amount of SLES (depending on initial and final concentration tested) by changing only the agitation speed. From this graph it is possible to observe that, for all concentration range, dissolution time decreases as function of the speed, in particular, a significant reduction can be observed in the first speed range from 30 to 500 rpm, then, especially for high concentration (from 15 to 20% w/v and from 20 to 25% w/v), dissolution time is almost constant or at least

doesn't change a lot; another significant speed change can be observed at 2000 rpm.

In most tested conditions, the blade does not come into contact with the SLES; this, as already explained in the section of materials and methods of this chapter, is placed on the bottom of the beaker and the stirring of the blade causes the movement of the solution in the beaker, but not the breaking of the SLES. For these conditions even if it is not possible to consider the process like purely diffusive, it is necessary to distinguish it from the case in which, when the agitation is high (>1000 rpm), the SLES detaches from the bottom and comes into contact with the blade; when this happens there is a fragmentation of the SLES in smaller pieces, what changes is substantially the surface of SLES in contact with the solution that facilitates the dissolution, significantly accelerating the process.

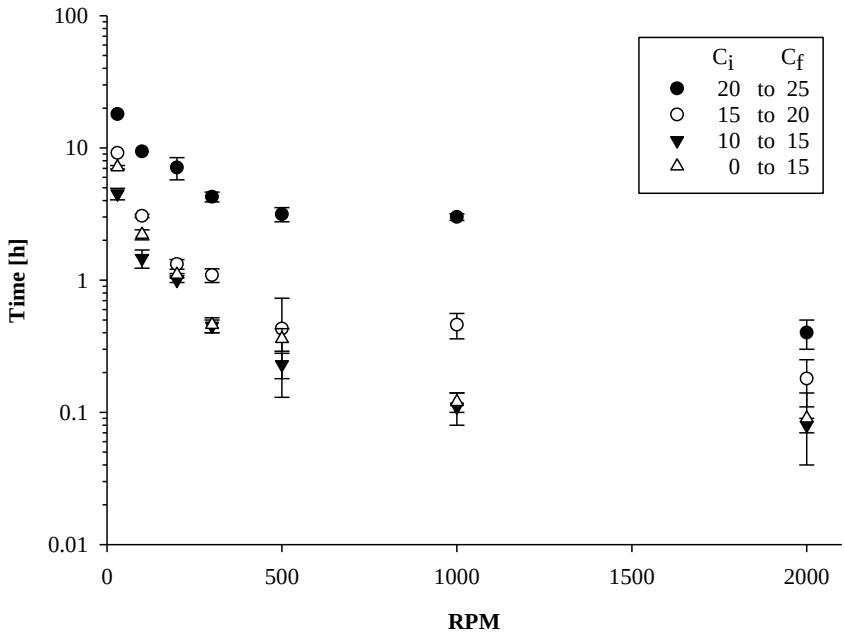

Figure 40 **Dissolution time of SLES in different bulk concentration and at different agitation speed.**

Moreover, another important result, that has to be highlighted, is the fact that, in these test, as well as in the dissolution test under flow on a single droplet, described in Chapter 3 (*Figure 30*), dissolution time changes a lot when initial bulk concentration is of 20% w/v; for all the other concentration range, there is a difference between all the conditions tested, but is not as evident as for this case.

Raman results

After having tested different speed for different concentration range, some of those conditions have been selected and repeated using a Raman tool to check the process over time. During experiments, Raman signal has been acquired. Raman signal is acquired in a frequency range from 1800 cm^{-1} up to 300 cm^{-1}, but only the area above the characteristic peak at 1300cm^{-1} has been measured; the ratio between this area and the one related to water banding for different concentration and 3 speed is reported in *Figure 41*.

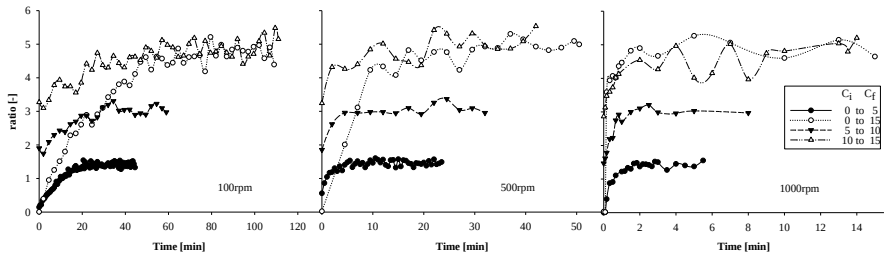

Figure 41 **Evolution over time of Raman signal for different concentration range and 3 speeds.**

In the beaker, while dissolution occurs, the probe measures the Raman signal emitted by the solution, especially at low speeds (100 and 500 rpm), there is no interference, only when the speed increases (> 1000 rpm) the measured signal can be lower; for this reason, and also to optimize the signal / noise ratio, in post process the area of the Raman signal is measured in the

range of interest and this is normalized by the value of the Raman signal associated with the banding of the water that does not change with the variation of the concentration. The ratio of these signals over time provides a very accurate estimate of the state of dissolution, it is possible to estimate what the concentration value reached by the solution is by observing the Raman signal.

In *Figure 41* it is possible to observe the evolution over time of this Raman signal ratio, that changes considerably according to the delta concentration between the initial bulk solution and the final concentration. Moreover, it is possible to observe the effect of the speed; the Raman signal follows perfectly the concentration in the bulk solution. When the stirring speed increases, the dissolution process takes place more rapidly, the amount of SLES which dissolves in the first moments of time is much higher and it is possible to read this also from the acquired Raman signal, the measured value turns out to be immediately higher as soon as the agitator is turned on.

Pilot plant tests

For the analysis of the data obtained from the tests in the pilot plant, the area under the peak at the frequency of 1560 cm^{-1} was evaluated, without considering the ratio of this value with respect to the intensity of the peak corresponding to the O-H banding. The reason for this choice lies in the fact that, as previously mentioned, in order to derive the concentration value from the Raman signal, it is possible to evaluate indistinctly one of the areas subtended to the peaks at the frequencies of 1560 and 1300 cm^{-1}, or the report can be evaluated, however, since the data related to the area in question are more precise, these have been used as a reference.

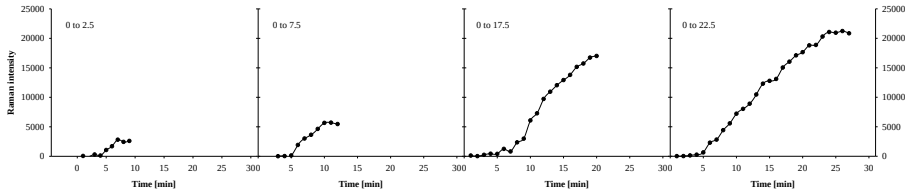

Figure 42 **Raman spectra of 4 different test, all starting from pure water to different final concentration.**

In *Figure 43* Raman spectra over time of the second step of 4 different tests are reported. It is evident that with raman it is possible to read even little concentration variation like it has been done in the second step of the tests. From these plots it is possible to read clearly how the slop of those curves is different from test to test; concentration increases differently changing initial concentration value.

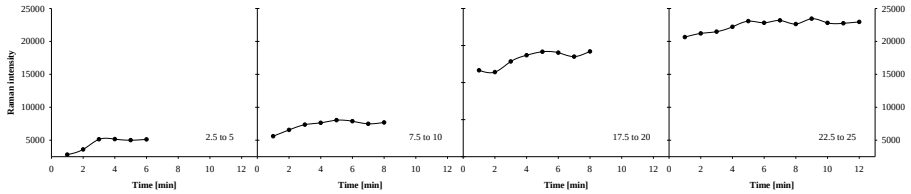

Figure 43 **Raman spectra of the second step of previous 4 test, starting from different bulk concentration with the addition of the same amount of SLES.**

Scale up results

In order to be able to scale up characteristic dissolution time from medium scale to pilot plant scale, both those experimental condition have been compared considering characteristic dissolution time, obtained by fitting of Raman data, as a function of Reynolds number.

For the medium scale set up, Reynolds number in a beaker can be calculated as

$$\frac{\mathrm{N} * D^2}{\eta}$$

Where:

- N is the speed (rpm)
- D is the blade diameter (cm)
- η is the viscosity (Pa*s)

For simplicity, for all the test, the viscosity was considered as the value corresponding to the average concentration of SLES solution.

The same relationship can be used for the batch system, and in this way it possible to compare data in the same diagram.

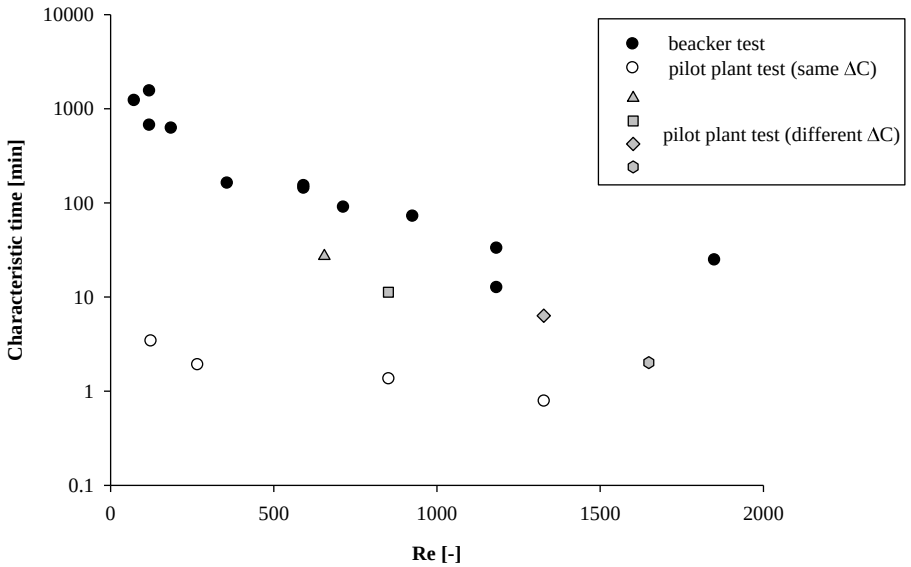

Figure 44 **Characteristic dissolution time of medium and pilot plant scale tests.**

In *Figure 44* black dots are characteristic time of all the conditions tested in beaker tests, white ones are data referring to the second step of all the test carried out in the pilot plant, where all the test have the same delta concentration, and finally grey dots with different shapes are from the first step of the test, these have different delta concentration.

4.4 Conclusions

For the study of the dissolution of the SLES on a medium scale, preliminary tests were carried out in the laboratory, in which the dissolution state was measured by monitoring the conductivity of the solution by means of a conductivity meter, from these tests it was possible to estimate a characteristic trend of dissolution time according to the dissolution rate. Subsequently an experimental campaign was carried out in which the dissolution time was calculated, as the stirring speed and the initial and final concentration of the solution vary, from these tests it is shown that the dissolution time decreases with increasing stirring speed, going from 30 to 500 rpm, then it remains almost constant up to 1000rpm. Comparing the tests to vary the initial concentration of the bulk solution, it is seen that the dissolution time increases markedly when the concentration of SLES in the solution is 20%, the same difference that had been noticed in the microfluidic tests, described in Chapter 3, from which it was possible to deduce that by increasing the concentration in the solution, the gradient force decreased and consequently, the dissolution time increased.

Some of those tests have been selected and a Raman probe was used to check the process over time. Raman is a good tool to check how the process is going on. By fitting the Raman data, it is possible to estimate a characteristic dissolution time, as a function of the speed and the concentration.

Subsequently, tests were carried out in the pilot plant, also for those test Raman data have been acquired to estimate the general trend.

In order to compare results obtained in beaker and ones in the pilot plant, all results have been plotted as a function of Reynolds number.

Characteristic dissolution time in the pilot plant test scales with the lab test results and particle size affect the characteristic time

Conclusions

In this work, the study of the dissolution of Sodium Lauryl Ether 3Sulfate (SLES) in water was carried out in both static and flow conditions, using a multi-technical approach, starting from the static study in the laboratory, to the tests carried out in the pilot plant.

A rheological characterization of the system under constant and oscillatory shear flow was performed which showed non-monotonic variations of different orders of magnitude in its viscosity and viscoelastic modules as a function of the surfactant concentration.

A simple multi-parameter model based on diffusion was developed, by means of which we were able to describe dissolution data from both stable and dynamic SLES.

Time-lapse microscopy observations on a disk-shaped SLES specimen in quiescent water showed that the water penetrates radially, thus taking to the sample a radially layered onion structure where each layer was characterized by a microstructure typical of a different one mesophase.

The results obtained using the various experimental and numerical approaches are all in great agreement, showing for the first time a complete analysis of the dissolution phenomena of complex surfactant pastes in static and flow conditions. The approach proposed here can provide useful support for the design and optimization of various industrial processes.

The first approach to dissolution was carried out in collaboration with two other research groups of the University of Naples, Federico II.

In particular, both for the part of the rheological characterization and the modeling one, we must thank the people who made these measures possible, Prof. Ing. Rossana Pasquino and Ing. Massimiliano Maria Villone.

Subsequently, an in-depth study of the static dissolution of the SLES was conducted. From the tests carried out the forward speed of the fronts was measured, from this measure it is clear that the transition from the hexagonal to the micellar phase is the slow step that dominates the temporal evolution of the whole process.

Furthermore, the size and shape of the air bubbles present in the sample was studied. As soon as the surfactant comes in contact with water, the sample appears to be subjected to a compressive stretching, as is evident from the analysis of bubble deformation. This phenomenon is also supported by the observation of the movement of particles used as a tracer. During the dissolution process, the phase equilibrium fronts move towards the center of the surfactant disc, when the bubbles are hit by the cubic phase, they undergo a compression, while they cross the hexagonal phase undergo a lengthening.

A possible explanation of the observed process can be attributed to the Marangoni effect. The Marangoni effect is associated with two surface phenomena, the motion in a fluid interface due to the local variation of the interfacial tension caused by differences in composition or temperature induced for example by a dissolution (or evaporation) of a solute, and therefore from the departure from equilibrium tension, produced by the dilatation of an interface.

For the first time, the SLES dissolution process was then studied by applying the flow effect and comparing the results between different solvents. In particular, the effect of the flow on dissolution has been

evaluated by the microscale of a single droplet of paste, but the aim is to extrapolate information that is not limited to the simple micro-fluidic cell, but could also be applied on an industrial scale optimizing the industrial processes.

From the experiments conducted, an attempt was made to trace a more general model of the characteristic parameter of the process, namely the dissolution time.

Firstly, it has been observed that the flow strongly influences the dissolution process; the dissolution time of the same surfactant drop under static conditions is significantly higher. By increasing the cutting speed, there is a considerable reduction in the dissolution time.

From the tests carried out it has been observed that the use of fibers, which lead to an increase in the viscosity of the system, has a positive effect on the dissolution. The characteristic times are reduced compared to the case in which the solvent is simply water and this reduction is even more marked when the percentage of these substances is higher. However, what can make the process significantly slower is an increase in bulk fluid concentration, which reduces the strength of the gradient and leads to a higher dissolution time.

For the study of the dissolution of SLES on a medium scale, preliminary tests were carried out in the laboratory, in which the dissolution state was measured by monitoring the conductivity of the solution by means of a conductivity meter, from these tests it was possible to estimate a characteristic trend of the dissolution time according to the dissolution rate. Subsequently an experimental campaign was conducted in which the dissolution time was calculated, since the stirring speed and the initial and final concentration of the solution vary, from these tests it is shown that the

dissolution time decreases with increasing the speed of stirring, going from 30 to 500 rpm, so it remains almost constant up to 1000 rpm. Comparing the tests to vary the initial concentration of the bulk solution, we see that the dissolution time increases considerably when the concentration of SLES in the solution is 20%, the same difference that had been detected in the microfluidic tests, described in Chapter 3 from which it was possible to deduce that by increasing the concentration in the solution, the force of the gradient decreased and, consequently, the dissolution time increased.

Some of these tests were selected and a Raman probe was used to control the process over time. Raman is a good tool for checking how the process is going. By adapting the Raman data, it is possible to estimate a characteristic dissolution time, as a function of speed and concentration.

Subsequently, tests were carried out in the pilot plant, also for those Raman test data were acquired to estimate the general trend.

To compare the results obtained in the beaker and those in the pilot plant, all the results were traced according to the Reynolds number. The characteristic dissolution time in the pilot plant test scales with laboratory test results and particle size influence the characteristic time.

Future work

From the point of view of static dissolution, the dynamics' complexity could be explored to explain the anomalous behavior of the tracer particles or the deformations of the air bubbles. Preliminary tests have already been carried out in which the static dissolution process was observed in a Cartesian geometry and, at the same time, placing side by side measurements performed with Raman microscopy.

With regard to the study of the dissolution in flow, the microfludic device used has proved to be an appropriate tool for studying, in a simple manner, the surfactant solvent interaction and the effect of the flow. In this regard, tests to vary the concentration of surfactant in solution and / or the variation of the flow could be carried out for a more general picture of the phenomenon. On the other hand, with the same device, different surfactants or the effect of more or less complex bulk solutions could be tested.

Finally, of great interest both from the scientific and industrial point of view, it would be a more detailed experimental campaign in the pilot plant, in order to evaluate the effect of the surfactant particle size, the effect of the shear and finally the use of bulk solutions that are more and more complex to evaluate the effect of chemical interaction between surfactant and solvent.

Appendix

Conductivity and spectrophotometry measurements

In order to study the static dissolution, in addition to the measurements performed with the timelapse microscopy, with the aim to try to obtain quantitative information about the process itself, coducibility and spectrophotometry measures have been done.

Considering the stock solution of SLES with an initial concentration of 70%, samples were prepared at different final concentration by diluting the initial sample with bidistilled water. The samples were prepared using a high precision balance and each sample was stirred with a mechanical stirrer until complete dissolution. With this procedure samples were prepared at 25%, 20%, 15%, at concentrations from 10 to 9% every 1%, 0.75%, 0.5%, 0.25%, 0.1%, 0.075%, 0.5%, 0.025%, 0.01 %, 0.001%

Conductivity measurement

The electrical conductivity of a material is due either to the presence of free electrons (as in the case of metals) or to free ions (as in the case of electrolyte solutions). In the first case we refer to electronic or metallic conductors, in the second case to electrolytic conductors. The electrical conductivity of an electrolytic conductor depends on its nature, temperature and its geometry with respect to the measuring electrodes; also the solvent exerts its influence on the conductivity values.

In this case, which concerns the electrolytic conductors, the electrical conductivity measures the ability of the ions to carry the electric current in an aqueous solution.

For each sample, conductivity measurements were carried out using an Eutech PC 2700 conductivity meter.

Spectrophotometry measurements

I_0 is supposed to be the intensity of the monochromatic light which affects a solution contained in a special cuvette. The solution absorbs in part the incident radiation, therefore at the exit of the cuvette its intensity is reduced to a value I. The absorption of light by the solution is defined by a dimensionless size, called absorbance (A), equal to the logarithm of the ratio of I_0/I which is defined by the Lambert Beer law, according to which, if a substance is able to absorb light, the absorbance of the solution is directly proportional to its concentration, at least for a certain range of values of the

$$\mathrm{A} = \mathrm{LC}\varepsilon$$

where:

- C it is the concentration of the solute able to absorb light;
- ε is the extinction coefficient, referred to a specific wavelength;
- L it is the length of the optical path.

For each prepared sample, the absorbance spectrum was measured by a Shimadzu pharmaspec uv-1700 spectrophotometer.

Theoretically, by analyzing the sample in a specific wavelength range, a spectrum should be obtained with a Gaussian pattern. The band should have a sufficiently narrow width and should have a peak in a neighborhood of a frequency at which the sample absorbs most. Moreover, the value of the peak, or in general of the measured absorbance, should not exceed the value of 2 units otherwise it would be interpreted as an artifact. Unfortunately, in practice, the analyzed sample did not show a behavior that could easily be interpreted with the traditional method. The pattern of the appearance is not clearly Gaussian, but has several peaks. In particular, a significant peak occurs at the value close to the full scale of the instrument (ie about 190 nm) and the measured absorbance value often also reaches 4 units. To try to interpret the spectra of the samples at different concentrations, they were analyzed using data analysis techniques. In this case the PCA (Principal Component analysis) was used. For this reason, for each sample with different concentration, not the absorbance at a specific wavelength, but the whole absorbance spectrum was measured.

The spectrophotometer used is double-beam. It has two housings, one for the sample cuvette and one for the white cuvette. White is a solution that is taken as a reference. Its value is automatically subtracted from the sample in order to measure the absorbance value related to the substances present only in the sample and not in the reference solution, ie that with which the sample is prepared. The cuvettes can be produced with special plastics able to let the radiation pass between 300 and 1000 nm, or they can be realized with higher quartz costs, which is transparent to the radiation even in the 190-300 nm range.

In the test performed quartz cuvettes were used, as the absorbance spectrum was calculated in a range of 190-350 nm. The spectrophotometer was connected to the computer via the UvProbe software.

Analysis of dissolution experiments

The static tests were carried out as described in paragraph X; in this case, however, the aim was to try to evaluate the presence in the solution of a concentration gradient as a function of the distance from the sample (compared to a central point z_0, made to coincide with the center of the surfactant disk, three equidistant points were defined z_1, z_2 and z_3, respectively at 2, 4 and 6 cm of distance from the center z_0, measured radially along the diagonal: in the tank, the SLES is placed first and immediately after the water, after a certain time 500 µl of solution have been taken, through a pipette, in points z_1, z_2 and z_3 (figure). This sample volume was chosen not to alter the concentration and the ratio between the amount of surfactant and added water.

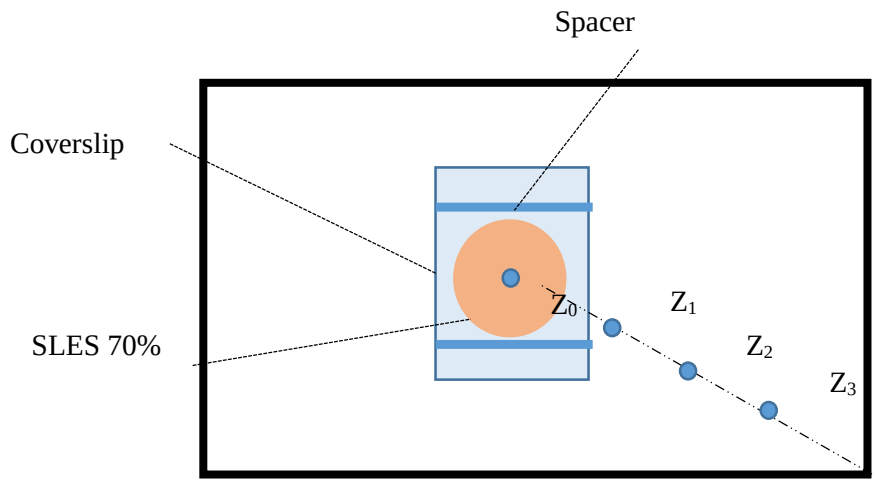

Figure 45 **Cartoon of static set up for conductivity measurements.**

The withdrawn aliquots of solution were inserted into 3 test tubes. In order to measure the conductivity value, it was necessary to further dilute the aliquots taken as the sensor of the conductivity meter is about 2 cm from the bottom of the tube and therefore the 500 µl is not sufficient. For this reason, 3 ml of bidistilled water were added to each tube in order to obtain

a useful volume to perform the measurement. From the value obtained for the diluted conductivity sample, the undiluted conductivity value is obtained from a material balance $C_i V_i = C_f V_f$

where:

- C_i is the conductivity of the undiluted sample;
- C_f is the conductivity of the diluted sample;
- V_i is the initial volume of the solution;
- V_f is the final volume of the solution.

For measurements with the spectrophotometer, instead, the aliquots of the withdrawn solution were diluted reaching a solution volume of about 1.3 ml.

Furthermore, once the aliquots were taken at different distances, the whole solution in the tank was inserted into another test tube and the conductivity of the whole solution was measured. The operations were repeated by taking samples at fixed time instants of 30, 60, 90 and 120 minutes. Each time the test was carried out ex novo. To check the accuracy of the results, every single test was performed 3 times for all the different moments of time.

Conductivity results

The conductivity value was measured 3 times for each sample and using the obtained values, a calibration line was constructed that associates a precise conductivity value to each SLES concentration value.

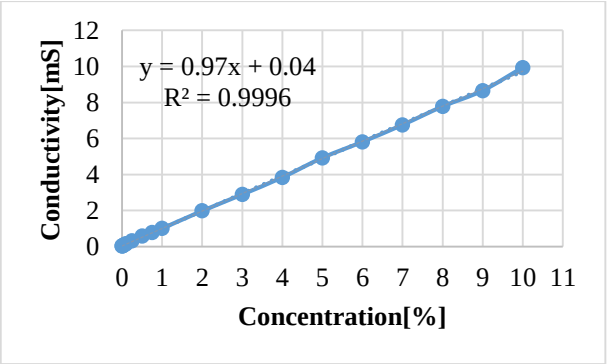

Figure 46 **Calibration curve Conducibility/Concentration from 0.001% up to 10%.**

From the calibration curve, the linear dependence between the conductivity and the concentration in the whole observed range is clearly evident.

Plotting the experimental data, the intercept value of the equation is obtained, i.e. the conductivity value at the point where the surfactant concentration is zero. At this point an intercept value equal to the conductivity value of the water should be reachd. The value get through the experimental measurements does not coincide with the value set by the calibration line. This difference is probably due to both the variation in the conductivity value of the water used, which varies between 2 µS and 14 µS, and the proximity of this particularly low value to the full scale of the instrument.

Spectrophotometry results

As mentioned before, for each sample, prepared at the different concentrations, the absorbance spectra were measured in the chosen wavelength range (190 ÷ 350 nm). The measurements were repeated 3 times. For each concentration the mean of the absorbance values measured

by the instrument was calculated, the values were averaged over the 3 tests and the standard deviation was calculated

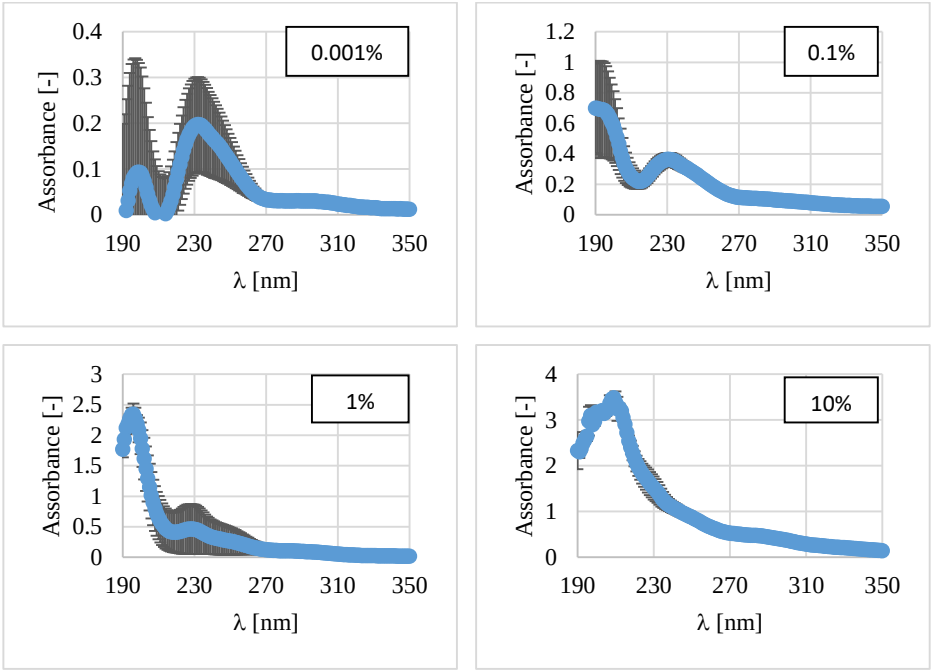

Figure 47 **Abrorbace spectra of SLES samples at different concentrations**

From these graphs it is noted that the spectra trend is qualitatively similar to low concentrations. In particular up to 0.25% we note the presence of two absorbance peaks at wavelengths at 190 and 230 nm. As the SLES concentration increases, the peak at 230 nm decreases until it disappears.

Moreover, for high concentrations, the peak value at 190 nm is amplified compared to the low concentrations, with values even higher than 3 units.

PCA analysis results

From the obtained spectra, a single wavelength value cannot be drawn out in correspondence of which there is an absorbance peak that is the same for the samples at the different concentrations. For this reason, a single

absorbance measurement cannot be performed to derive the concentration. Consequently, in order to try to obtain information from the spectra obtained, these values have been analyzed through data analysis techniques. In particular, the PCA (Principal Component analysis) was used through the JMP software.

For each spectrum obtained at the different concentrations two parameters were extracted: the main component 1 and the main component 2. The first seems to have a strong concentration dependence. Therefore, by plotting the main component for all the concentrations, a sufficiently linear trend is seen, above all for concentrations higher than 1%.

Observing the graphs, in particular those in the logarithmic scale, it is noted that at low concentrations (<1%) there is no linearity, indeed the values are almost constant.

The values obtained for the 3 tests considered are averaged and the trend of the mean value is plotted.

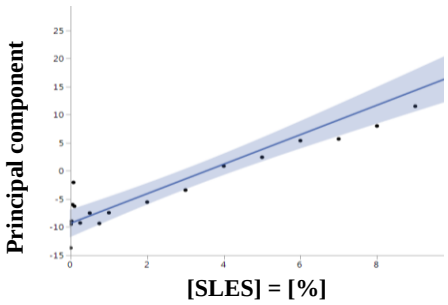

Figure 48 **PCA analysis: Main component over SLES concentration.**

Conductivity vs Spectrophotometry

The general objective is to use the data obtained from the analysis of the absorbance and / or the conductivity to analyze the dissolution tests. The

analyzes made with the absorbance are more complex from the point of view of the preparation and analysis of the data that are not reliable for concentrations lower than 1%. The line created through the conductivity measurements, on the other hand, gives an immediate link between concentration and conductivity. The latter technique has the disadvantage that the aliquot must be diluted particularly, so that the measure can be altered taking aliquots less than 100ml. Vice versa, in the analysis of the spectrophotometer, since the minimum volume to make the measurement is smaller, it must be less diluted, so that aliquots of lower solutions could be taken. In conclusion, considering that at least in the dissolution tests carried out in the laboratory, concentrations are very low, the conductivity measurement was preferred.

Dissolution test results

By monitoring the static dissolution process during time and over space, it can be seen clearly from the graph in the figure that the concentration value, read promptly near the surfactant disk, increases over time until the expected value, that should be read after dissolution, is reached (the red horizontal line represents the expected value); however, moving away radially from the center, the concentration tends to decrease, which is expected for the initial times, but which persists even at longer times, even when the dissolution process has occurred completely and the whole surfactant has passed into solution.

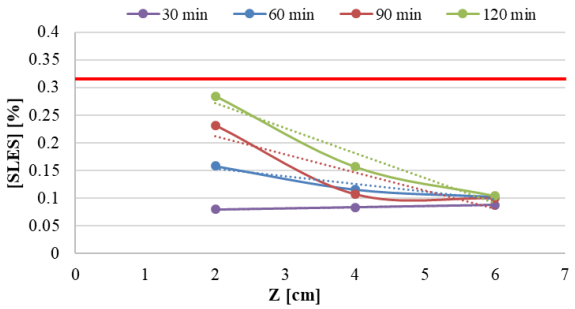

Figure 49 **Concentration value obtained from conductivity measurements as a function of distance.**

The graph below also shows that the amount of surfactant dissolved in solution in the initial times is very low, so the conductivity value measured initially is close to that of water. Instead, after a melting time of 120 minutes, the concentration value obtained experimentally from the conductivity measurements is close to the theoretical value obtained from the material balance.

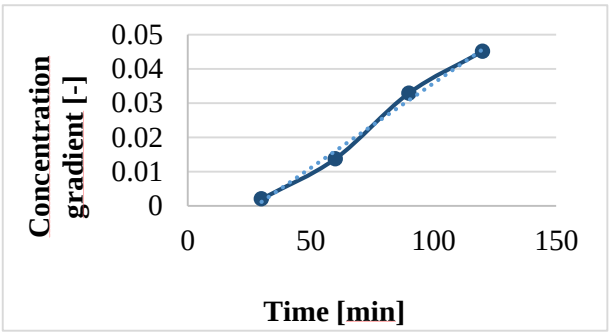

Figure 50 **External driving force grows over time**

List of figures

Figure 1 Surface tension as function of SLES concentration[7] 12
Figure 2 CMC for several kinds of surfactants. 13
Figure 3: CMC and solubility curves of SDS in water 14
Figure 4: Optical properties of liquid crystals. Isotropic lamellar phase (L_1), hexagonal phase (H_1), cubic phase (V_1), lamellar phase (L_α).....18
Figure 5: Classical surfactant in water phase diagram 19
Figure 6: structure of the mielines at the interface for a solvent/surfactant system at different times 24
Figure 7 Phase diagram of LAS/AES/H_2O system at 25°C.....28
Figure 8 (Not to scale) schematic drawings of the rheological setup (a), the optical setup (b), and of the computational domain for static dissolution numerical simulation (c). 38
Figure 9 Viscosity curves for various SLES concentrations (see legend for details).....41
Figure 10 Viscoelastic moduli as function of angular frequency for 15%wt (a), 50%wt (b) and 70%wt (c) SLES. 42
Figure 11 a) Magnitude of the complex viscosity at a frequency of 1 rad/s (black circles) and steady viscosity at a shear rate of $1s^{-1}$ (white circles) as a function of SLES concentration. b) Elastic modulus (black circles) and loss modulus (white circles) at a frequency of 1 rad/s as a function of SLES concentration. The dashed lines represent morphological transitions: L_1 micellar phase, H hexagonal phase, V_1 cubic phase, L_a lamellar phase. ...43
Figure 12 Optical experiments. During the dissolution of a surfactant disk, it is possible to visualize 4 different phases: an internal core of lamellar phase ($L_{\square}$), a first ring of cubic phase (V_1), a second ring of hexagonal phase (H), and a more external micellar phase (L_1). The interfaces between the phases shrink radially as dissolution goes on. 45
Figure 13 Radial displacements of the L_a-V_1, V_1-H, and H-L_1 phase-transition fronts during the dissolution of a 4-mm-radius 70%wt surfactant disk. Symbols: experimental measurements; Curves: Least Squares fits by a Fickian diffusion model (the estimated parameters reported in the legend). 46
Figure 14 Maximum of the torque modulus |M| measured by the parallel plate rheometer during the dissolution of a 4-mm-radius surfactant disk.

Pink circles: experimental measurements, cyan triangles: numerical simulations 50
Figure 15 Radial displacements of the phase-transition fronts during the dissolution of a 4-mm-radius surfactant disk paste with an initial concentration equal to 50%wt (a) and 60%wt (b). Symbols: experimental measurements, curves: Least Squares fits by a Fickian diffusion model (the estimated parameters are reported in each panel on the right). 51
Figure 16 The cartoon on the left shows the experimental setup: the sample is optically scanned by mosaic imaging (center), the composite image is reconstructed in post-processing (right). 56
Figure 17 SLES morphology. Images were acquired using Zeiss Pascal confocal microscope at different magnification (10x a and e, 20x c, 63x oil b and f). Conoscopic images (d) were acquired using a Canon EOS60D camera, removing the eyepieces, and observing the sample down the microscope tube. 58
Figure 18 Typical time evolution of a SLES disk during static dissolution experiments. The image at t=0 was acquired from the raw sample, before water addiction. Other images were acquired at different times. All images were acquired using Zeiss Axiovert 200 microscope, 5x, by mosaic scanning. 60
Figure 19 Position of interfaces between different phases during dissolution. Red circles, green up triangles and blue down triangles represent the boundaries between hexagonal and micellar (H-L), cubic and hexagonal (V-H) and lamellar and cubic (Lα-V) phases, respectively. All interfaces decrease their radial position as a function of time, the outer (H-L) is the slower. 62
Figure 20 Anomalous motions of beads inside the sample during dissolution. Zoom of initial instant time and cartoon with complexively description. 65
Figure 21 Water and SLES flow among different phase transitions. 67
Figure 22 Bubbles' deformation through different phases. In order to visualize the presence of the interfaces, image (a) was acquired with cross polarizers. is shown in sequence, these images were acquired in the bright field. 69
Figure 23 Bubble size and deformation parameters during the dissolution process. 72
Figure 24 Experimental setup cartoon, home-made microfluidic device (side view on the bottom), with syringe pump to push the solvent inside and beaker at the end to collect the out coming flow. 79

Figure 25 viscosity of SLES solution at different concentrations. 82
Figure 26 rheology of cellulose fibers solution at different concentration.....83
Figure 27 Viscosity of cellulose fibers solution, at fixed shear rate.....87
Figure 28 Example images of dissolution over time of SLES in water at different flow rates.....88
Figure 29 Evolution over time of SLES in water at different flow rates...90
Figure 30 Dissolution time of SLES at the same flow rate in water with different solution.....91
Figure 31 Panel with effect of fibers concentration on dissolution for each tested flowrate.....92
Figure 32 dissolution time over shear stress for all the conditions tested. 93
Figure 33 surfactant disc paste droplet during dissolution under flow, the edge between phases are highlighted with two lines. 96
Figure 34 Detail of surfactant filament forming in the flow direction. 97
Figure 35 Medium scale dissolution test of SLES in water, dissolution is measured with a conductivity meter. 100
Figure 36 Pilot plant setup cartoon. 101
Figure 37 Raman spectra of SLES in water solution at different concentrations. The calibration curve obtained by spectra analysis is reported in the top right of the figure.....103
Figure 38 conductivity curves during the dissolution of SLES in water at 3 different agitation speed.....104
Figure 39 Characteristic dissolution time at different speed, estimated by conductivity measurements.....105
Figure 40 Dissolution time of SLES in different bulk concentration and at different agitation speed.....106
Figure 41 Evolution over time of Raman signal for different concentration range and 3 speeds. 107
Figure 42 Raman spectra of 4 different test, all starting from pure water to different final concentration.....109
Figure 43 Raman spectra of the second step of previous 4 test, starting from different bulk concentration with the addition of the same amount of SLES. 109
Figure 44 Characteristic dissolution time of medium and pilot plant scale tests. 110

References

1. Poulos, A. S.; Jones, C. S.; Cabral, J. T., Dissolution of anionic surfactant mesophases. *Soft Matter* **2017,** *13* (31), 5332-5340.
2. Laughlin, R., Correction. The Aqueous Phase Behavior of Surfactants. *Journal of the American Chemical Society* **1995,** *117* (42), 10603-10603.
3. Li, H.; Dang, L.; Yang, S.; Li, J.; Wei, H., The study of phase behavior and rheological properties of lyotropic liquid crystals in the LAS/AES/H2O system. *Colloids and Surfaces A: Physicochemical and Engineering Aspects* **2016,** *495* (Supplement C), 221-228.
4. Attwood, D.; Florence, A. T., *FASTtrack Physical Pharmacy*. Pharmaceutical Press: 2012.
5. Myers, D., *Surfactant science and technology*. John Wiley & Sons: 2005.
6. Bai, J. Dissolution rates of surfactants and granules. Rice University, 2003.
7. Nowak, E.; Kovalchuk, N. M.; Che, Z.; Simmons, M. J., Effect of surfactant concentration and viscosity of outer phase during the coalescence of a surfactant-laden drop with a surfactant-free drop. *Colloids and Surfaces A: Physicochemical and Engineering Aspects* **2016,** *505*, 124-131.
8. Warren, P.; Prinsen, P.; Michels, M., The physics of surfactant dissolution. *Philosophical Transactions of the Royal Society of London A: Mathematical, Physical and Engineering Sciences* **2003,** *361* (1805), 665-676.
9. Warren, P.; Buchanan, M., Kinetics of surfactant dissolution. *Current opinion in colloid & interface science* **2001,** *6* (3), 287-293.
10. Miller-Chou, B. A.; Koenig, J. L., A review of polymer dissolution. *Progress in Polymer Science* **2003,** *28* (8), 1223-1270.
11. Kosswig, K., Surfactants. *Ullmann's encyclopedia of industrial chemistry* **2000**.
12. Larsson, K., Cubic lipid-water phases: structures and biomembrane aspects. *The Journal of Physical Chemistry* **1989,** *93* (21), 7304-7314.
13. Zeng, X.; Liu, Y.; Impéror-Clerc, M., Hexagonal close packing of nonionic surfactant micelles in water. *The Journal of Physical Chemistry B* **2007,** *111* (19), 5174-5179.
14. Yaghmur, A.; De Campo, L.; Sagalowicz, L.; Leser, M. E.; Glatter, O., Emulsified microemulsions and oil-containing liquid crystalline phases. *Langmuir* **2005,** *21* (2), 569-577.
15. Stabilized, D. L. L. C. P., by a Hydrophobically Modified Cellulose Almgren, Mats; Borne, Johanna; Feitosa, Eloi; Khan, Ali; Lindman, Bjoern. *Langmuir* **2007,** *23* (5), 2768-2777.
16. Razumas, V.; Larsson, K.; Miezis, Y.; Nylander, T., A Cubic Monoolein− Cytochrome c− Water Phase: X-ray Diffraction, FT-IR, Differential Scanning

Calorimetric, and Electrochemical Studies. *The Journal of Physical Chemistry* **1996,** *100* (28), 11766-11774.
17. Caboi, F.; Nylander, T.; Razumas, V.; Talaikyté, Z.; Monduzzi, M.; Larsson, K., Structural effects, mobility, and redox behavior of vitamin K1 hosted in the monoolein/water liquid crystalline phases. *Langmuir* **1997,** *13* (20), 5476-5483.
18. Hargreaves, T., *Chemical Formulation: An Overview of Surfactant-Based Preparations Used in Everyday Life.* 2003.
19. Valois, P.; Verneuil, E.; Lequeux, F.; Talini, L., Understanding the role of molar mass and stirring in polymer dissolution. *Soft matter* **2016,** *12* (39), 8143-8154.
20. Peppas, N. A.; Wu, J.; von Meerwall, E. D., Mathematical modeling and experimental characterization of polymer dissolution. *Macromolecules* **1994,** *27* (20), 5626-5638.
21. Chen, B.-H.; Miller, C. A.; Walsh, J. M.; Warren, P. B.; Ruddock, J. N.; Garrett, P. R.; Argoul, F.; Leger, C., Dissolution rates of pure nonionic surfactants. *Langmuir* **2000,** *16* (12), 5276-5283.
22. De Luca, A. C.; Rusciano, G.; Pesce, G.; Caserta, S.; Guido, S.; Sasso, A., Diffusion in polymer blends by Raman microscopy. *Macromolecules* **2008,** *41* (15), 5512-5514.
23. Jonas, A.; De Luca, A. C.; Pesce, G.; Rusciano, G.; Sasso, A.; Caserta, S.; Guido, S.; Marrucci, G., Diffusive Mixing of Polymers Investigated by Raman Microspectroscopy and Microrheology. *Langmuir* **2010,** *26* (17), 14223-14230.
24. Laughlin, R.; Munyon, R., Diffusive interfacial transport: a new approach to phase studies. *Journal of Physical Chemistry* **1987,** *91* (12), 3299-3305.
25. Rodgers, T. L.; Mihailova, O.; Siperstein, F. R., Dissolution of Lamellar Phases. *The Journal of Physical Chemistry B* **2011,** *115* (34), 10218-10227.
26. Gerritsen, H.; Caffrey, M., Water transport in lyotropic liquid crystals and lipid-water systems: Mutual diffusion coefficient determination. *Journal of Physical Chemistry* **1990,** *94* (2), 944-948.
27. Macosko, C. W., Rheology: Principles, Measurements, and Applications. Wiley-VCH ed.; Oct 1994.
28. Tiddy, G. J., Surfactant-water liquid crystal phases. *Physics reports* **1980,** *57* (1), 1-46.
29. Kahlweit, M.; Strey, R., Phase Behavior of Ternary Systems of the Type H2O Oil Nonionic Amphiphile (Microemulsions). *Angewandte Chemie International Edition in English* **1985,** *24* (8), 654-668.
30. Brinker, C. J.; Lu, Y.; Sellinger, A.; Fan, H., Evaporation-induced self-assembly: nanostructures made easy. *Advanced materials* **1999,** *11* (7), 579-585.
31. Rodgers, T. L.; Cooke, M.; Siperstein, F. R.; Kowalski, A., Mixing and dissolution times for a cowles disk agitator in large-scale emulsion preparation. *Industrial & Engineering Chemistry Research* **2009,** *48* (14), 6859-6868.
32. Ascione, F.; Caserta, S.; Guido, S., The wound healing assay revisited: A transport phenomena approach. *Chemical Engineering Science* **2017,** *160*, 200-209.

33. Quarteroni, A.; Sacco, R.; Saleri, F., *Numerical mathematics*. Springer Science & Business Media: 2010; Vol. 37.
34. Buchanan, M.; Egelhaaf, S. U.; Cates, M. E., Dynamics of interface instabilities in nonionic lamellar phases. *Langmuir* **2000,** *16* (8), 3718-3726.
35. Cristini, V.; Guido, S.; Alfani, A.; Bławzdziewicz, J.; Loewenberg, M., Drop breakup and fragment size distribution in shear flow. *Journal of Rheology* **2003,** *47* (5), 1283-1298.
36. Tucker III, C. L.; Moldenaers, P., Microstructural evolution in polymer blends. *Annual Review of Fluid Mechanics* **2002,** *34* (1), 177-210.
37. Caserta, S.; Guido, S., Vorticity banding in biphasic polymer blends. *Langmuir* **2012,** *28* (47), 16254-16262.
38. Bąk, A.; Podgórska, W., Investigation of drop breakage and coalescence in the liquid–liquid system with nonionic surfactants Tween 20 and Tween 80. *Chemical Engineering Science* **2012,** *74* (Supplement C), 181-191.
39. Crank, J., *The mathematics of diffusion*. Oxford university press: 1979.
40. Jonas, A.; De Luca, A.; Pesce, G.; Rusciano, G.; Sasso, A.; Caserta, S.; Guido, S.; Marrucci, G., Diffusive mixing of polymers investigated by Raman microspectroscopy and microrheology. *Langmuir* **2010,** *26* (17), 14223-14230.
41. Rosen, M. J.; Kunjappu, J. T., *Surfactants and interfacial phenomena*. John Wiley & Sons: 2012.
42. Vasaturo, A.; Caserta, S.; Russo, I.; Preziosi, V.; Ciacci, C.; Guido, S., A novel chemotaxis assay in 3-D collagen gels by time-lapse microscopy. *PloS one* **2012,** *7* (12), e52251.
43. Scharf, T., *Polarized light in liquid crystals and polymers*. John Wiley & Sons: 2007.
44. Caserta, S.; Reynaud, S.; Simeone, M.; Guido, S., Drop deformation in sheared polymer blends. *Journal of Rheology (1978-present)* **2007,** *51* (4), 761-774.
45. Taylor, G. I., The Formation of Emulsions in Definable Fields of Flow. *Proc Roy Soc A* **1934,** *146* (858), 501-522.
46. Santiago-Rosanne, M.; Vignes-Adler, M.; Velarde, M. G., Dissolution of a drop on a liquid surface leading to surface waves and interfacial turbulence. *Journal of colloid and interface science* **1997,** *191* (1), 65-80.
47. Porter, D.; Savage, J. R.; Cohen, I.; Spicer, P.; Caggioni, M., Temperature dependence of droplet breakup in 8CB and 5CB liquid crystals. *Physical Review E* **2012,** *85* (4), 041701.